QUANTITATIVE SIMULATION OF BACKSCATTER FROM TISSUE AND BLOOD FLOW FOR ULTRASONIC TRANSDUCERS

A Thesis
Presented to
The Academic Faculty

By

Bernard Shieh

In Partial Fulfillment
Of the Requirements for the Degree
Master of Science in the
School of Mechanical Engineering

Georgia Institute of Technology

August, 2015

QUANTITATIVE SIMULATION OF BACKSCATTER FROM TISSUE AND BLOOD FLOW FOR ULTRASONIC TRANSDUCERS

Approved by:

Dr. Karim Sabra
School of Mechanical Engineering
Georgia Institute of Technology

Dr. Levent Degertekin
School of Mechanical Engineering
Georgia Institute of Technology

Dr. Julien Meaud
School of Mechanical Engineering
Georgia Institute of Technology

Date Approved: March 3rd, 2015

TABLE OF CONTENTS

LIST OF TABLES

Page

LIST OF FIGURES

Page

SUMMARY

This master's thesis discusses the development of simulation tools for the quantitative simulation of ultrasound backscatter from tissue and blood flow for arbitrary transducer arrays. These simulation tools have potential applications in the field of medical ultrasonics, with particular attention to the areas of transducer design and optimization, beamforming and array processing, and image reconstruction. The work presented here is part of a broader research effort to develop comprehensive simulation tools for the characterization of imaging performance of capacitive micromachined ultrasound transducers.

This thesis is organized in the following manner. In Chapter 1, a brief overview of the state of the art for diagnostic medical ultrasound and introduce fundamental concepts relevant to ultrasound image reconstruction is provided. In Chapter 2, an approach to quantitative simulation of tissue backscatter based on the application of tissue speckle models is described. In Chapter 3, details of how this approach can be used to investigate problems in ultrasonic flow imaging are provided. In Chapter 4, extensions to this work and related investigations that have been left to future studies are outlined.

CHAPTER 1

INTRODUCTION AND BACKGROUND

To better motivate the work presented here, we present a brief overview of the necessary background material. In Section 1.1, an introduction to the use of diagnostic ultrasound in medicine is provided. A review of recent developments to the area of ultrasonic flow imaging and their application to cardiac imaging is given in Section 1.2. In Section 1.3, the fundamental concepts of imaging and array processing are given.

1.1 Ultrasound in medicine

The foundations of medical ultrasound originated first with the discovery of piezoelectricity by the brothers Pierre Curie and Jacques Curie in 1880, and subsequently by the intense research efforts, spurred on by World War II, to develop technologies for submarine detection (SONAR, SOund NAvigation And Ranging) and aircraft detection (RADAR, RAdio Detection And Ranging). These technologies, which worked on the basic principle of sending and receiving pulsed acoustic and/or electromagnetic waves off of distant objects, were then adapted for the purpose of probing the human body.

Although ultrasound had been used in medicine at the time for therapeutic purposes, the first physician to utilize utlrasound for diagnostic purposes was Karl Dussik, who in 1947 created the first ultrasound image in a procedure called "hyperphonography" [1]. Dussik created a rudimentary image of the brain using a through-transmission technique from two transducers placed on each side of the head. The image created was a two-dimensional mapping based on the strength of the signal from the receiving transducer.

Other researchers explored the use of echo-ranging techniques, analogous to those used in SONAR and RADAR, by looking at waves reflected back towards the transmitting transducer. This was driven in part by the invention of the supersonic reflectoscope, a compact ultrasound device invented in the 1940s by Floyd Firestone for detecting flaws in metals. The reflectoscope operated by transmitting a series of ultrasonic pulses and displaying on an oscilloscope the received echos as a function of time, producing what was called an "A-scan" (also "A-mode" and "A-line"). In 1952, it was shown by John Wild and John Ried that A-scans of the breast could be used to differentiate between benign and malignant tissue and to detect cysts. The A-scan was followed by the devel-

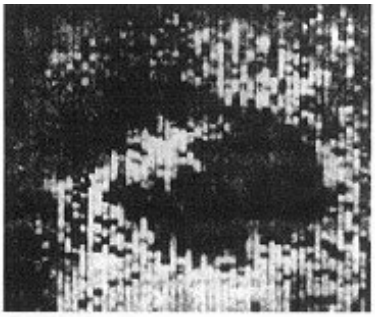

Figure 1: One of the first ultrasound images, a hyperphonogram was created by placing two transducers on each side of the head and measuring the through-transmission signal amplitude [1].

opment of "B-mode" (also "B-scan" and "Brightness-mode") images which were two-dimensional mappings produced by scanning the transducer by either freehand or mechanical positioning systems and displaying the corresponding A-scans from each position alongside one another. This technology, in combination with the tremendous progress of integrated circuit technology, eventually lead to the modern incarnations of phased array transducers and real-time gray-scale images used in ultrasound systems now.

Today, ultrasound imaging is a ubiquitous part of the modern diagnostic toolbox. It has widespread applications to many areas of medicine, including angiology, cardiology, nephrology, urology, and obstetrics. For example, ultrasound is often used to diagnose arterial and venous diseases, and for grading stenoses. It is also used to guide needle placement for delivery of anesthetics and for guiding surgeries such as biopsies. Moreover, ultrasound is often preferred over other imaging modalities, such as x-ray computed tomography (CAT), magnetic resonance imaging (MRI) and optical coherence tomography (OCT), because it is non-invasive, non-ionizing, inexpensive, and has good penetration depth in the body.

Modern ultrasound scanners come in relatively manageable sizes; typical systems are roughly the size of a desktop computer but even laptop-sized and cell-phone sized portable systems are now commercially available. These scanners come with a variety of detachable transducers which are optimized to image different parts of the body. Modern systems also come loaded with a large catalog of imaging modes which change the way data is acquired, processed, and visualized. Aside from the A-mode and B-mode operations which were described previously, these modes include: M-mode (several A-mode or B-mode images are acquired in succession, producing a video which can display tissue motion), elastography (a class of distortion-based techniques used to measure mechanical properties of tissue such as stiffness), doppler (a class of techniques to measure the velocity of moving tissue), harmonic (tissue is excited at the fundamental frequency and the transducer is used

Figure 2: A three-dimensional image of a fetus produced from 3D/4D modes available on modern commercial ultrasound scanners [2].

to record signals from harmonic frequencies generated by the tissue), and 3D/4D (three-dimensional images and videos reconstructed from multiple slice images). These advanced modes are often used in displayed as overlays on top of standard B-mode images so that both the anatomical information and the additional information are shown together.

1.2 Recent advances in cardiac ultrasound imaging

Ultrasound is a critical tool for the detection of heart diseases and for surgical planning and guidance of procedures in the heart, such as mitral valve repair and transcatheter aortic valve replacement. Cardiac ultrasound imaging (also called echocardiography) is the application of ultrasound techniques to imaging of the heart. In the present state of the art there are three methods for probing the heart: transthoracic echocardiography (TTE), transesophageal echocardiography (TEE), and intracardiac echocardiography (ICE).

In a transthoracic echocardiogram, a transducer is placed on the chest of a patient and images of the heart are obtained through the chest wall. TTE, the least invasive of all the methods, requires only external access to the chest to obtain images of all four chambers of the heart and to assess valvular function. The quality of TTE images can be limiting in some cases due to the small acoustic windows available for imaging through the chest, a problem that is exacerbated in patients that are obese and also in patients with lung disease. TTE is also limited in its ability to image the back of the heart due to poor ultrasound penetration through the chest.

To overcome these limitations, a physician may opt for a transesophageal echocardiogram instead. In TEE, a specialized transducer is inserted into the patient's esophagus and the ultrasound image is acquired from the backside of the heart. Because the heart is located just millimeters from the

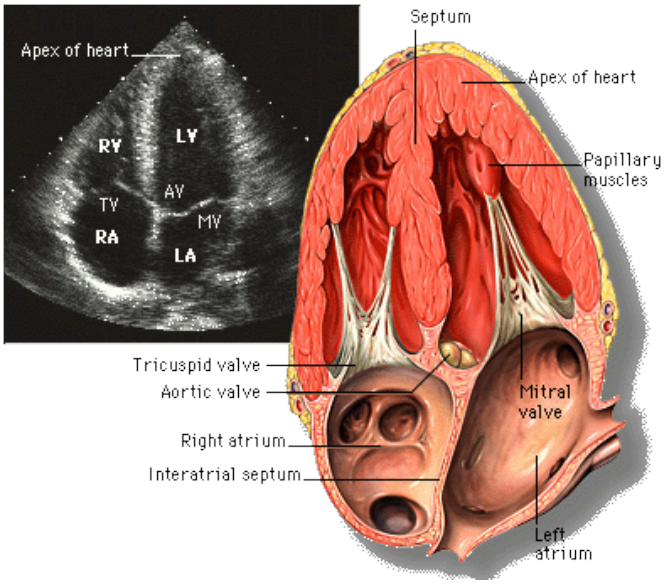

Figure 3: An example of a transthoracic echocardiogram displaying an apical four chamber view with a corresponding anatomical diagram of the heart [3].

esophageal wall, the images produced in TEE are much clearer than in TTE. The downside, however, is that the TEE procedure is significantly more invasive than that for TTE; the insertion of TEE probes in the esophagus can cause discomfort and may require sedation or local anesthesia.

Intracardiac echocardiography, the most invasive of the procedures, consists of special millimeter-sized ultrasound transducers placed on the tip of a catheter that is then inserted into the heart, usually via the inferior vena cava, and into the right atrium. ICE produces the most direct image of the heart interior and valvular function and can be performed without anesthesia–properties that make ICE a viable alternative to TEE for interventional procedures.

In all three methods, the standard for imaging is B-mode which produces real-time anatomical images representing two-dimensional slices of the heart. To improve the clarity of the image, B-mode images of the heart are often augmented with real-time doppler images showing blood flow information. This information can be used to identify the location of valves and to assess the severity of leakages. More recently, 3D/4D imaging modes which display volume-rendered views of the heart have become available on commercial systems for use in TTE and TEE.

While echocardiography has become an established tool for cardiologists, there remains a number of technical limitations which are areas of intense research. Image quality, especially in TEE and ICE, are constrained by hardware and by diffraction-limited resolution, the latter of which is related directly to the available lateral dimensions of the transducer. Interpretation of cardiac B-mode images is often difficult and relies on the skill of the operator to both orient the transducer to obtain

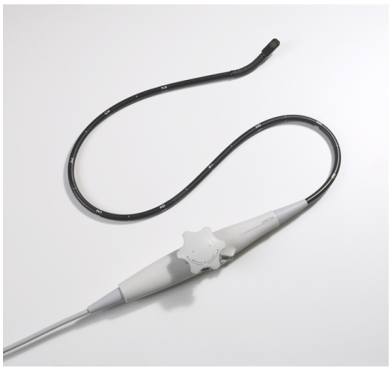

Figure 4: A transesophageal echocardiogram probe. The probe is inserted into the patient's esophagus and used to image the backside of the heart through the esophageal wall [4].

meaningful slices and to correctly interpret the resulting images. While 3D/4D images can alleviate some of these concerns, the increased rendering demands for reconstructing volumes comes with the cost of severely reduced frame rate and increased presence of motion artifacts.

Doppler modes also face a number of technical challenges limiting its clinical utility. Due to technical limitations in the way flow information is reconstructed (seen details in Chapter 3), doppler images can only display flow velocities that are oriented either toward or away from the transducer. This makes quantitative assessment of flow speeds and volume loss difficult. Real-time doppler information is also restricted to smaller regions of the full B-mode view due to the significant computational requirements of reconstruction.

1.3 Imaging and array beamforming fundamentals

The vast majority of modern medical ultrasound transducers are phased arrays–a technology adapted from SONAR and RADAR. The primary advantage of phased arrays is the ability to finely control the direction of pressure waves emanating from the transducer (i.e., beamsteering)–a feature that allows for complete images to be reconstructed from a single static position of the transducer. We outline here the basic principles of phased array operation and how they are applied in medical ultrasound.

Phased arrays are composed of several individual transduction elements (usually at least 64) which are wired electronically so that each element is individually addressable (or often multiplexed in some fashion). These arrays are typically created using single piezoelectric crystals (e.g. PZT) that are then physical segmented into individual elements via dicing. Elements can be arranged in a variety of patterns, the most common of which are the linear array–arranged along a single line–and the matrix array–arranged in a two-dimensional cartesian grid. The purpose of having

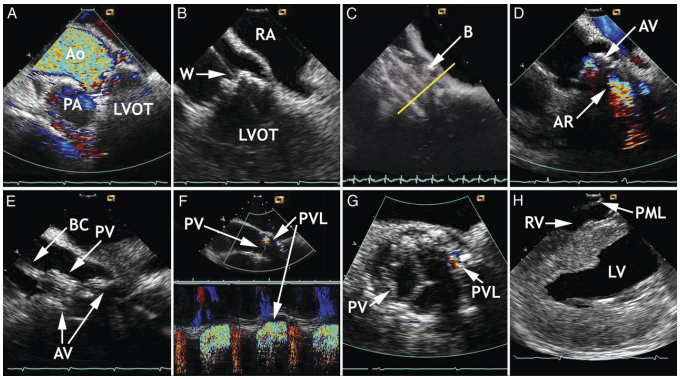

Figure 5: Many different intracardiac echocardiogram views with doppler flow information overlaid in color [5].

several individually addressable elements spread out over space is to provide the array with spatial discrimination and therefore the ability to control the directivity in real-time.

Take, for example, the transmission of a pressure pulse into the medium. The array is excited by a short, broad-band electrical pulse which is sent to each element of the array with a specific time delay. The delays can be set to compensate for the time-of-flight necessary for a pulse from an individual element to reach a specific point in space. This "focusing" of the array leads to constructive interference at the desired point in space, resulting in a higher pressure intensity in a smaller volume. The same principle can be applied during receive operation to provide the array with a spatially-dependent gain.

The focusing ability of an array is governed by the principles of wave diffraction. From a purely image resolution perspective, it is desirable to have: (1) an array with a large lateral dimension relative to the wavelength (the size of the aperture), (2) an array with small spacing between elements relative to a wavelength (the pitch), and (3) a very short-duration excitation pulse. A large lateral dimension improves the ability of the array to focus waves to a point, thereby improving the lateral resolution. A small element to element pitch improves the spatial sampling of the wavefield and ensures that the array can discriminate between incoming waves coming from all directions of interest. Insufficient sampling of the wavefield will result in spatial aliasing that appear as grating lobes in the image. In practice many other factors must be taken into consideration when designing an array, but these principles serve as a general rule of thumb.

A standard pulse-echo B-mode image is created using the principles of focusing in both transmit and receive operation. The array is focused in transmit along a specific line and focused in receive along the same line, resulting in an A-scan. In processing, the envelope-detected signal is computed and plotted as a function of time, with pixel brightness used as an indicator of signal amplitude.

This process is repeated for an adjacent line in the medium until the entire imaging domain has been covered. When the A-scans from each firing are plotted next to each other with time/depth represented on one axis and A-scan number represented on the other axis, a B-mode image is formed.

A full image may require hundreds of firings, depending on the density of the A-scans and the total field of view (FOV). Generally, the maximum rate at which A-scans can be collected, called the pulse repetition frequency (PRF), is limited only by the travel time in the medium (a 12 cm depth at a sound speed of 1540 m/s will have a maximum acquisition rate of 6400 Hz). This is the reason why volumetric images used in 3D/4D modes suffer from low frame rates; interrogating a 60° by 60° FOV with 1° line density in this way would require 3600 lines.

Reducing the number of firings needed to obtain full images is an area of active research. Most promising are synthetic aperture techniques (described in more detail in Chapter 3) which use fewer transmit firings and data acquired simultaneously on all receive elements to reconstruct images. This effectively shifts the computational load of beamforming from the electronics to the post-processing step, employing GPU-accelerated algorithms to reconstruct different regions of the image simultaneously. Although synthetic aperture techniques generate enormous amounts of data, increasing throughput and processing power of modern computers are improving the possibility of seeing these techniques employed clinically.

CHAPTER 2

QUANTITATIVE SIMULATION OF TISSUE BACKSCATTER

Ultrasound probes have been adopted clinically for imaging many areas of the body, including the heart, liver, kidney, and arteries. Faced with a variety of different imaging environments, ultrasound probes must often be optimized for performance in specific applications. This is especially true for catheter-based solutions such as ICE and IVUS, where imaging performance is strongly dependent on the strength of backscatter from tissue due to significant limitations in device size, electronics, and signal-to-noise ratio. The ability to accurately simulate tissue backscatter from ultrasound arrays is thus a useful tool for estimating performance and can potentially become an integral step in the design process.

This chapter discusses a method for the quantitative simulation of tissue backscatter. The method is based on an application of the Rayleigh speckle model to the linear systems model for acoustic fields. In Section 2.1, an overview of the linear systems model and its implementation in existing software is presented. In Section 2.2, a discussion of tissue backscatter and an overview of the Rayleigh speckle model are provided. In Section 2.3, the method is presented along with implementation details for Field II and validation results from a simulated experiment. Finally, examples of how this method can be applied to characterize array performance are presented in Section 2.4.

2.1 The linear systems model for the simulation of acoustic fields

The linear systems model for acoustic fields [11] [12] is a simple but powerful framework for the numerical calculation of emitted pressure fields from complex transducer apertures. It accurately captures diffraction effects and can handle features relevant to ultrasound systems, such as: element phasing, element apodization (shading), arbitrary-shaped elements, lossy media, and arbitrary time-domain excitation.

Compared to full-wave models [13] which solve special wave equations on discretized spatial and temporal grids, the linear systems model does not capture non-linear propagation effects due to the medium and cannot model multiple scattering in a simple way. Fortunately, most basic applications of ultrasound imaging are with respect to the fundamental frequency and in weakly-scattering media (where the Born approximation is sufficient). The primary advantage of the linear systems model

over these more complicated acoustic field models is in computation and memory efficiency. When simulating fields from dense arrays and in large volumes, these can quickly become prohibitive for their practical implementation.

At the heart of the linear systems model is the concept of spatial impulse response $h(\vec{r}, t)$, which is closely related to the Rayleigh integral for radiation from sources on a 2D plane. It is defined as

$$h(\vec{r}, t) \equiv \iint_S \frac{\delta(t - \frac{|\vec{r}-\vec{r}_s|}{c})}{2\pi|\vec{r}-\vec{r}_s|} \, \mathrm{d}S \tag{1}$$

Here, $\vec{r}$ and $\vec{r}_s$ are the observation and source vectors, respectively, c is the sound speed in the medium, $\delta(t)$ is the dirac impulse function, and the integration is carried out over the surface S of all active sources on the transducer. From herein, the subscripts tx and rx are used to denote variables related to either transmit or receive operation of the transducer, respectively.

The delaying and scaling of the impulse function in the spatial impulse response captures the diffraction of the waves due to the vibration of the transducer surface. Typically, we are interested in calculating pressure fields from a velocity excitation separable in time and space, i.e. $u(\vec{r}_s, t) = w(\vec{r}_s)u(t)$ where $w(\vec{r}_s)$ is a continuous apodization function and $u(t)$ is an arbitrary excitation of the normal surface velocity in time. An expression for the pressure in this case is given by

$$p(\vec{r}, t) = \rho_0 \frac{d}{dt} u(t) * \iint_S \frac{w(\vec{r}_s)\delta(t - \frac{|\vec{r}-\vec{r}_s|}{c})}{2\pi|\vec{r}-\vec{r}_s|} \, \mathrm{d}S \tag{2}$$

The spatial impulse response in this case depends on the apodization function and is not amenable for numerical computation. A straight-forward simplification is to discretize the active transducer surface into smaller geometric elements of uniform normal velocity. As long as the discretization is sufficiently fine, a continuous apodization function can be approximated in this manner. We may also be interested in additional time-delays τ_{tx} for each geometric element to incorporate phasing for the purpose of beamforming. The pressure in this case is simply a sum over the weighted and delayed spatial impulse responses for the geometric elements.

$$p(\vec{r}, t) = \rho_0 \frac{d}{dt} u(t) * \sum_n [w_n \delta(\tau_{tx,n}) * h_n(\vec{r}, t)] \tag{3}$$

where n specifices the geometric element in question and the sum is carried out over all such elements of the array.

Spatial impulse responses can be calculated efficiently for a variety of geometric shapes, such as

lines and rectangles [14]. This provides flexibility in how complex array surfaces can be discretized for numerical computation. For additional efficiency, far-field approximations can be used which are valid near the transducer surface as long as the geometric elements are sufficiently small.

The linear systems model can be extended by modeling the electromechanical transduction of the transducer as a linear system as well. We can define an electromechanical impulse responses for the transducer from one physical quantity to another, e.g. $e_{v\to a}(t)$ is the electromechanical response from voltage to normal surface acceleration. Incorporating this into the expression for pressure yields

$$p(\vec{r}, t) = \rho_0 v_{tx}(t) * e_{v\to a}(t) * \sum_n [w_n \delta(\tau_{tx,n}) * h_n(\vec{r}, t)] \tag{4}$$

where $v_{tx}(t)$ represents the voltage excitation applied to the transducer during transmit operation. The pressure from an apodized and phased array can therefore be calculated by a set of convolution products.

2.1.1 Field II and other acoustic field simulators

A number of ultrasound field simulation programs based on the linear systems model have been developed by the academic community. These include Ultrasim (University of Oslo) [15], DREAM (Institut d'Electronique de MicroÃľlectronique et de Nanotechnologie) [16], and Field II (Technical University of Denmark) [17]. Of the simulation programs currently maintained, Field II in particular has been used extensively by researchers, with applications including evaluation of image reconstruction technique [18], assessment of Doppler flow algorithms [19], and characterization of transducer performance [20]. Due to its widespread adoption in the ultrasound community, Field II was chosen (with certain modifications which will be motivated later) for the simulation studies in this work.

Field II is written in C++ with a front end MATLAB interface (via MEX-files). Details of its implementation of the linear model have been reported in a series of papers [21] [20] [17]. It supports the definition of arbitrary array shapes, apodization and phasing based on the basic equation described in (4). Additionally, Field II supports frequency-dependent fluid attenuation using a minimum-phase model [22].

Notably, the program extends the basic linear model by providing functions to calculate the full pulse-echo response (i.e., from excitation voltage to receive voltage). The simulation of the receive operation of the transducer is carried out in a reciprocal fashion to the transmit operation. To

understand why this is valid, consider the calculation of the mean pressure $\overline{p}_r(t)$ on a transducer surface of area S_{rx} due to a monopole source of power W at location $\vec{r}$ in the far-field.

$$\overline{p}_r(t) = \frac{1}{S_{rx}} \left(\frac{\rho_0 c W}{2\pi} \right)^{1/2} \iint_{S_{rx}} \frac{\delta(t - \frac{|\vec{r}_s - \vec{r}|}{c})}{|\vec{r}_s - \vec{r}|} \, \mathrm{d}S_{rx} = \frac{2\pi}{S_{rx}} \left(\frac{\rho_0 c W}{2\pi} \right)^{1/2} h_{rx}(\vec{r}, t) \tag{5}$$

The spatial impulse response can therefore be used to capture diffraction to and from a point in space, corresponding to transmit and receive operation of the transducer, respectively.

To tie the transmit and receive operations together, Field II uses a single amplitude scaling factor A which represents a selectable contrast ratio that one may encounter between two different scattering mediums. Full pulse-echo calculation in Field II from transmit voltage $v_{tx}(t)$ to receive voltage $v_{rx}(t)$ is therefore carried out using the following expression

$$v_{rx}(t) = \; v_{tx}(t) * \rho_0 e_{v \to a}(t) * h_{tx}(\vec{r}, t) \; * A \cdot h_{rx}(\vec{r}, t) * e_{a \to v}(t) \tag{6}$$

This approach is limited in a number of ways. First, the strength of backscattered waves from tissue generally have a strong dependence on frequency [23] [24] [25].

Second, a simple scaling factor does not tie simulated data to physical units on an absolute scale. To do so, the calculation procedure described by (6) should be related to a physical scattering model. We explore this problem in more detail in the next section.

2.1.2 A simple scattering model for Field II

The calculation of pressure at single points in the domain using a retarded-time approach in the linear systems model suggests that it can be easily combined with a simple linear scattering model [26]. Consider a single spherical scatterer of diameter much smaller than a wavelength. The scatterer can be treated as an idealized point located at the scattering center $\vec{r}$. We consider (in the frequency domain) a simple multiplicative scattering function $G(\theta, \phi, f)P(\vec{r}, f)$ which represents a spherically-symmetric scattered wave with the possibility of an angular and frequency-dependent amplitude. The form of the scattering function can be treated mathematically as an additional potential term in the linear wave equation derived by assuming small perturbations in the ambient sound speed and density [26]. For a collection of scatterers located at positions $\vec{r}_n$ with corresponding scattering functions $G_n(\theta, \phi, f)$, this formulation leads to the following problem:

$$\nabla^2 P(\vec{r}, f) + k^2 P(\vec{r}, f) = \sum_n G_n(\theta, \phi, f) P(\vec{r}_n, f) \tag{7}$$

We consider a number of simplifications to make this problem tractable.

First, we consider successive perturbed solutions for the pressure a la the Born expansion, which holds approximately for weakly-scattered fields. Let the total field be represented as a sum of an incident field and scattered field, where it is assumed that $|P_s| << |P_i|$.

$$P(\vec{r}, f) = P_i(\vec{r}, f) + P_s(\vec{r}, f) \tag{8}$$

The incident field is defined as the field present in the absence of all scatterers (i.e. the incident field satisfies the homogeneous wave equation). In the Born expansion, approximate solutions are arrived at using successive substitutions, starting with the incident field:

$$P^{(0)}(\vec{r}, f) = P_i(\vec{r}, f) \tag{9}$$

$$P^{(1)}(\vec{r}, f) = P^{(0)}(\vec{r}, f) + \sum_n G_n(\theta, \phi, f) P^{(0)}(\vec{r}_n, f) \tag{10}$$

$$P^{(2)}(\vec{r}, f) = P^{(1)}(\vec{r}, f) + \sum_n G_n(\theta, \phi, f) P^{(1)}(\vec{r}_n, f) \tag{11}$$

$$\vdots$$

In the first Born approximation $P^{(1)}$, the incident field is used in place of the total field to calculate the scattered field and no multiple scattering is accounted for. In the second Born approximation $P^{(2)}$ an additional term is present which accounts for first-order multiple scattering. Each successive iteration adds an additional term which takes into account an additional order of multiple scattering. The first Born approximation is adequate for our purposes (the justification for this choice will be provided in more detail in the next section).

Second, we consider simplifications to the scattering functions G_n. It is useful to define a differential scattering cross-section $\sigma_d(\Omega, f)$ which represents the power scattered into a unit solid angle from a target due to an incoming plane wave of unit intensity. We can also define a total scattering cross-section as the total power scattered over all solid angles.

$$\sigma_t(f) = \int \sigma_d(\Omega, f)\, \mathrm{d}\Omega \tag{12}$$

In pulse-echo ultrasound imaging, we are primarily concerned with scattered waves that return to the transducer. For this case, we define a backscattering cross-section $\sigma_{bs}(f)$ which is simply the differential cross-section evaluated in the direction exactly opposing the incoming wave. As long

as the angular variation of the scattered field over the solid angles subtended by the transducer is small, we can assume the following scattering function:

$$G_n(\vec{r}, f) = \sqrt{\sigma_{n,bs}(f)} \tag{13}$$

Third, since Field II and the linear systems model are based on a time-domain impulse response approach, we should convert the formulated scattering model into this framework. Frequency-dependent quantities can be replaced by time-dependent functions and products replaced by convolutions. The excitations used in pulse-echo ultrasound are typically very short, e.g. 1 to 2 cycles of a 5 MHz pulse. Because of this, we can safely neglect the effect of the incident field on the transducer during receive operation. This yields the following expression for the received pressure field averaged over the receive aperture of a transducer $\overline{p}_r(t)$:

$$\overline{p}_r(t) = p_i(\vec{r}_n, t) * \sum_n \sqrt{\sigma_{n,bs}(t)} * \frac{2\pi}{S_{rx}} h_{rx}(, t) \tag{14}$$

Finally, the mean pressure over the receive aperture is related to the normal acceleration of the front face by $\frac{\partial}{\partial t}\overline{p}_r(t) = \rho_0 c\, \vec{a}(t) \cdot \vec{n}$. Combing these ideas together, we relate the scattering model to the calculation procedure in Field II:

$$v_{rx}(t) = \; v_{tx}(t) * \rho_0 e_{v\to a}(t) * h_{tx}(\vec{r}, t) \; * \sum_n \sqrt{\sigma_{n,bs}(t)} * \frac{2\pi}{\rho_0 c S_{rx}} \frac{\partial}{\partial t} h_{rx}(\vec{r}, t) * e_{a\to v}(t) \tag{15}$$

Implicit in this formulation is the assumption that the transducer's presence has no effect on the scattered field. At the other extreme, we may consider the transducer to act as a hard baffle, resulting in a doubling of the pressure over the receive aperture. In either case, the error will not be more than 3 dB.

2.2 Ultrasonic backscatter from tissue

The scattering of ultrasonic waves in tissue is a complex process that can encompass a wide range of length scales due to the variety of structures present in the body. Ultrasound images may be composed of specular reflections (from bone, vascular tissue and other interfaces that are much larger than the wavelength) and speckle reflections (from the constructive and deconstructive interference of sub-wavelength inhomogeneities in soft tissue). As in the latter case, images of soft tissue can be thought of abstractly as mappings of relative backscattered intensity from tissue,

where the granularity and texture of the image is related to the underlying tissue structure and to characteristics of the transducer. This texture is known as speckle noise and is a phenomenon that is encountered in radar as well.

A number of models have been developed to describe the statistics of ultrasound speckle in its various regimes. These speckle models attempt to describe the statistics of the envelope-detected pressure by treating the generation of speckle in images as a stochastic process. The first of these models used a Rayleigh probability distribution function (PDF) to successfully describe speckle in the "fully-developed" regime [27]. Since then, generalizations of the Rayleigh model have been introduced which cover a wider-range of speckle regimes: the K-distribution [28], generalized K-distribution [28], and the homodyned K-distribution [29]. Other alternative models have also been investigated, including the Nakagami distribution [30] and the generalized Nakagami distrubtion [29]. These latter models describe the speckle statistics for a wider range of tissues beyond the diffuse case, at the expense of increased complexity (two and three-parameter distributions instead of one in the Rayleigh case). For example, they can successfully describe speckle in the case of low scatterer number density and in cases where there is a strong coherent component due to ordered structure in the medium.

2.2.1 The Rayleigh speckle model

The Rayleigh speckle model predicts that the enevelope-detected pressure at the transducer will follow a Rayleigh PDF. To understand this, consider a collection of point scatterers randomly distributed in space. The pressure seen on the transducer at any given instant in time will contain backscattered contributions from scatterers confined to a single resolution volume (also called the isochronous volume). The contributions from the resolution volume will sum together at the same instant in time, but may interfere constructively or destructively based on their phase.

When the point scatterers are distributed randomly in space with a sufficient number of scatterers per resolution volume, the summation of the pressure from each scatterer can be modeled by a random walk of a fixed-magnitude phasor in the complex plane. The magnitude of each phasor is equal to the instantaneous pressure amplitude that each scatterer contributes, where it is assumed that the incident intensity is approximately constant over the resolution volume such that the step size of the random walk is constant. The angle of the phasor is equal to the phase of each contribution, where the randomness of the scatterer positions leads to a uniform probability for the phase over the range $[0, 2\pi]$. Summing the contribution from each scatterer and taking the envelope is equivalent

to summing these complex phasors and taking the magnitude of the result–i.e. a random walk in the complex plane. The number of steps in the walk is equal to the number of scatterers in the resolution volume.

If the number of steps in the walk is sufficiently large, the instantaneous pressure amplitude received by the transducer P is described by a Rayleigh distribution, where the scale parameter α is related to the individual pressure contribution from each scatterer (the step size) P_1 and the number of contributing scatterers (number of steps) N_s. Expressions for the probability density function $p(P)$ and the mean envelope-detected pressure $\langle P \rangle$ are given by

$$p(P) = \frac{P}{2\pi\alpha^2} exp\left(-\frac{P^2}{2\alpha^2}\right) \tag{16}$$

$$\langle P \rangle = \alpha\sqrt{\frac{\pi}{2}} = \frac{P_1}{2}\sqrt{\pi N_s} \tag{17}$$

$$\alpha^2 = \frac{N_s P_1^2}{2} \tag{18}$$

The probability density function for the intensity amplitude $p(I)$ and its mean $\langle I \rangle$, which can be derived from a change of variables, follows an exponential distribution.

$$p(I) = \frac{\rho_0 c}{\alpha^2} exp\left(-\frac{\rho_0 c I}{\alpha^2}\right) \tag{19}$$

$$\langle I \rangle = \frac{\alpha^2}{\rho_0 c} = \frac{N_s P_1^2}{2\rho_0 c} \tag{20}$$

The mean intensity can be rewritten in terms of the backscattering cross-section $\sigma_{bs,1}$ of each individual scatterer, the incident intensity I_i, which is assumed to be the same at each scatterer, and the mean distance R between the transducer and the scatterers.

$$P_1^2 = 2\rho c \sigma_{bs,1} \frac{I_i}{R^2} \tag{21}$$

$$\langle I \rangle = N_s \sigma_{bs,1} \frac{I_i}{R^2} \tag{22}$$

2.2.2 Backscattering coefficient

It is convenient to introduce here the concept of backscattering coefficient $\eta_{bs}(f)$ (BSC), which is defined by the following volume integral:

$$\sigma_{bs}(f) = \int_V \eta_{bs}(f)\, \mathrm{dV} \tag{23}$$

$\eta_{bs}(f)$ is a frequency-dependent characteristic of tissue which represents the expected backscattered power when a volume of tissue is insonified by an incident plane wave of unit intensity. It provides an indicator of the average ability of a particular tissue to scatter waves back toward the transducer. This is useful for characterizing and differentiating between various types of tissue because it provides information on not only the expected backscattered power, but also how that power changes over different frequencies of insonification.

In practice, measuring BSC of a tissue sample requires special methods since the backscattered power will depend strongly on transducer diffraction and other properties. Because of its potential for tissue characterization, BSC for many common tissues have been documented in the literature, including blood, vascular tissue, myocardium, liver, kidney, dermis and fat.

Backscattering coefficient can be incorporated into the Rayleigh speckle model by adjusting the mean backscattered intensity predicted by the statistics in (19) (20) and to match a desired backscattering coefficient spectrum. When the backscattering coefficient is approximately constant over an insonified volume V_{res}, an expression for the backscattered intensity amplitude at the transducer is given by

$$\langle I \rangle = \eta_{bs}(f) V_{res} \frac{I_i}{R^2} \tag{24}$$

Comparison of (24) with (22) and defining the scatterer number density $n_s = N_s / V_{res}$ reveals that

$$\eta_{bs}(f) = n_s \sigma_{bs,1}(f) \tag{25}$$

In other words, the backscattering coefficient for an aggregation of randomly distributed point scatterers is simply the mean backscattering cross-section per unit volume. This is an expected result; the coherent addition should be zero, on average, due to the random phase of the scatterers, leaving only the incoherent summation of their backscattered pressures.

2.3 Quantitative representation of tissue in the linear systems model

In the previous section, it was shown that the Rayleigh speckle model can be implemented by simulating a sufficiently large number of point scatterers randomly located in space. These point scatterers should have a backscattering cross-section in proportion to a desired backscattering coefficient of tissue by the scatterer number density. Furthermore, the simulation should be performed by summing the individual contributions from each scatterer linearly, i.e. using a single-scattering model. Because the linear systems model is also based on single scattering, it is possible for the

Rayleigh model to be implemented exactly into simulation.

An accurate application of this idea must also take into account implementation details that may be specific to a given simulation program. In the case of Field II, limitations in how scattering is handled necessitate an additional post-processing step. This additional step must also take into account important physical quantities that are omitted. Here we outline the steps necessary steps required for a proper implementation in Field II.

Recall that the calculation for pulse-echo in Field II ties the transmit operation and receive operation together using a scalar contrast ratio A:

$$v_{rx}(t) = \; v_{tx}(t) * \rho_0 e_{v\to a}(t) * h_{tx}(\vec{r}, t) \; * A \cdot h_{rx}(\vec{r}, t) * e_{a\to v}(t) \tag{26}$$

The equivalent expression needed to incorporate a single-scattering model was derived in (15), which was:

$$v_{rx}(t) = \; v_{tx}(t) * \rho_0 e_{v\to a}(t) * h_{tx}(\vec{r}, t) \; * \sum_n \sqrt{\sigma_{n,bs}(t)} * \frac{2\pi}{\rho_0 c S_{rx}} \frac{\partial}{\partial t} h_{rx}(\vec{r}, t) * e_{a\to v}(t) \tag{27}$$

Comparison of (26) and (27) clearly shows that Field II's use of a scalar amplitude A is insufficient to capture frequency-dependent backscattering cross-section. Furthermore, the factor $\frac{1}{\rho_0 c}\frac{\partial}{\partial t}$, a result of defining the receive electromechanical response from normal acceleration to voltage ($a \to v$), is omitted. To simulate a frequency-dependent backscattering cross-section in Field II an additional convolution (filter) step must be introduced. The built-in behavior of Field II is bypassed by setting $A = 1$ and a filter $b(t)$ is applied in post-processing. The filter handles the missing factors and (25) is used to relate the individual cross-sections to the bulk characteristic of specific tissues.

$$b(t) = \frac{2\pi}{\rho c S_{rx}} \frac{\partial}{\partial t} \sqrt{\frac{\eta_{bs}(t)}{n_s}} \tag{28}$$

Since the receive electromechanical response is an input defined by the user, it is perfectly valid to use $e_{p\to v}$ in place of $e_{a\to v}$. Then,

$$b(t) = \frac{2\pi}{S_{rx}} \sqrt{\frac{\eta_{bs}(t)}{n_s}} \tag{29}$$

The filter $b(t)$ can be implemented in many ways, the simplest of which is to use finite impulse response (FIR) filters in conjunction with zero-phase filtering.

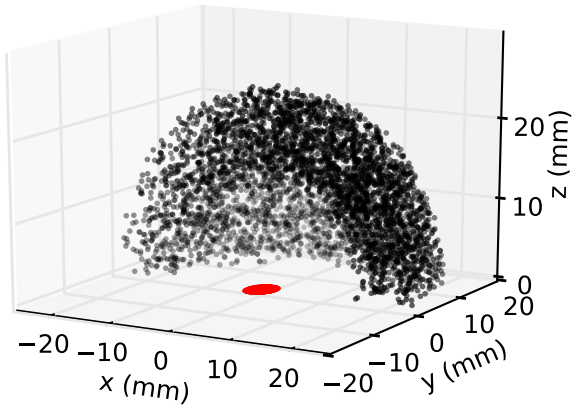

Figure 6: Cross-section of the hemispherical scattering volume and the focused piston array used for simulation of a backscattering coefficient measurement.

2.3.1 Validation using a simulated backscattering coefficient measurement

To demonstrate the validity of the proposed methodology, a simulation of a standard BSC measurement experiment was carried out in Field II using a formulation derived from expressions and methods outlined by Chen et al. [26]. An accurate assessment of BSC based on pulse-echo methods must take into account transducer characteristics such as electronic gains and diffraction corrections over the insonified volume. These additional factors are often simplified by comparison with a backscatter measurement from a standard reference case (e.g., a perfect planar reflector or a calibrated phantom). For the transducer, we assume a single element, spherically-focused piston transducer. From Chen et al. we can derive a general equation for BSC measurement using an arbitrary reference case:

$$\eta_{bs}(f) = \frac{\langle |v_{rx}(r \in V; f)|^2 \rangle}{|v_{ref}(f)|^2} \cdot \frac{|P_{ref}(f)|^2 / |P_{tx}(f)|^2}{l \cdot \overline{D}_s(r \in V, f)} \tag{30}$$

By time-gating the pulse-echo receive voltage for the unknown sample and the reference case, the insonified volume is approximately limited to a hemispherical volume of length l corresponding to the duration of the time gate. For the unknown sample, $\langle |v_{rx}(r \in V; f)|^2 \rangle$ is the spectral power of the time-gated receive voltage averaged over many speckle realizations and $\overline{D}_s(r \in V, f)$ is the mean diffraction correction of the transducer over the insonified hemispherical volume. For the reference case, $|v_{ref}(f)|^2$ is the spectral power of the receive voltage, $|P_{ref}(f)^2|$ is the mean pressure amplitude over the transducer aperture, and $|P_{tx}(f)| \equiv \rho_0 c U(f)$ is the characteristic pressure amplitude during

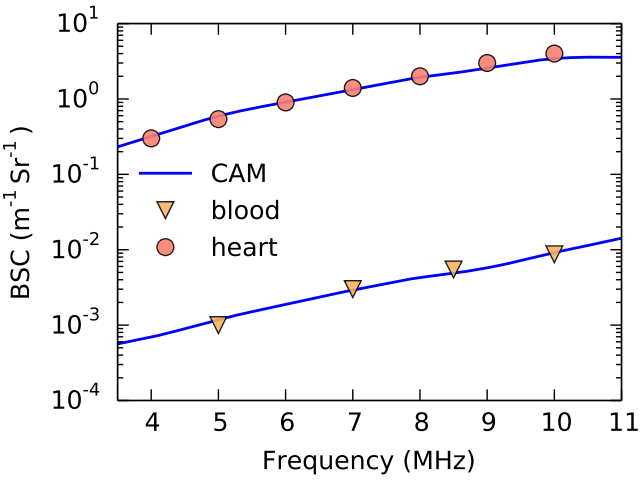

Figure 7: Comparison of backscattering coefficient measured from simulation using CAM with the desired empirical values for blood and canine myocardium.

transmit, where $U(f)$ is the mean normal velocity amplitude over the transducer aperture.

While it is common to use a planar reflector as a reference case, it is impractical to define such reflectors quantitatively in Field II. Instead, a point reference of known backscattering cross-section $\sigma_{bs,ref}$ is used, where an expression for the mean received pressure amplitude over the transducer aperture is also provided by Chen et al.

$$|P_{ref}(f)| = |P_{tx}(f)| \cdot \frac{2\pi}{kS_R} \cdot \sqrt{\sigma_{bs,ref}} \cdot |D_{ref}(r_0, f)|^2 \tag{31}$$

$D_{ref}(r_0, f)$ is the diffraction correction function of the transducer evaluated at its focus. It is related to the Fourier transform of the spatial impusle response defined in (1) by $H(\vec{r}, f) = (-1/ik)D(\vec{r}, f)$. The diffraction correction at the focus of a spherically-focused transducer is simply

$$|D_{ref}(r_0, f)| = \frac{ka^2}{2r_0} = \frac{kS_R}{2\pi r_0} \tag{32}$$

where a is the radius of the active element, S_R is the active surface area, and r_0 is the focal distance of the transducer.

Further simplification can be made, as per Chen et al., if it is assumed that the gate length is much smaller than the focal distance of the transducer such that $\overline{D}_s(\vec{r}, f)$ is approximately equal to the diffraction correction integrated over a hemispherical surface with radius r_0. This leads to the following simplification

$$\overline{D}_s(r \in V, f) \cong \frac{\pi a^2}{r_0^2}(0.46) \tag{33}$$

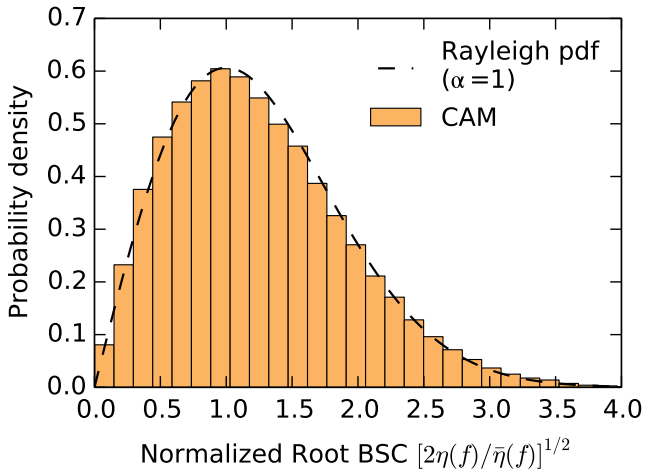

Figure 8: Speckle statistics from a simulated backscattering coefficient measurement based on CAM. The statistics match the expected Rayleigh probability density function with unity scaling parameter.

Finally, substituting (31), (32), and (33) into (30) yields an expression for the approximate measurement of BSC using a spherically-focused transducer and a point reference case:

$$\eta_{bs}(f) = \frac{\langle |v_{rx}(r \in V; f)|^2 \rangle}{|v_{ref}(f)|^2} \cdot \left(\frac{k}{2\pi r_0}\right)^2 S_R \cdot \frac{\sigma_{bs,ref}}{0.46\, l} \tag{34}$$

This is the formulation used for the simulated measurements and herein will be referred to as the Chen et al. approximate measurement (CAM).

To simulate CAM in Field II, point targets were placed randomly within a hemispherical volume of mean radius 2 cm with a number density of 20 targets/mm^3. A focused piston transducer was defined with a diameter of 5 mm, a focal distance of 2 cm (f-number 4), and a 6 MHz center frequency with 150% fractional bandwidth. RF data produced from a pulse-echo simulation of this setup (see Figure 6) constituted a single speckle realization. To mimic the stochastic nature of speckle, this simulation was repeated for a total of 1000 instances, with each instance composed of a new random target distribution. For the reference measurement, a single point was placed at the focal distance and an identical transducer was used. In all these simulations, a Field II target amplitude of 1 was used.

Finite impulse response (FIR) filters were designed using (28) to match BSC spectra for blood (human, 8% hematocrit) [9] and myocardium (canine) [8] measured experimentally from excised samples. These filters were applied separately in post-processing to produce two sets of data. For the reference case, an FIR filter designed to give a flat spectral response with unit backscattering cross-section was used.

Finally, BSC was calculated using the CAM formulation in (34)–the results are shown in Figure 7. Comparison of the CAM values to the desired empirical BSC spectra show excellent agreement, indicating that the methodology proposed here is consistent and capable of capturing frequency-dependent backscatter in Field II. Furthermore, the mean backscattered intensities are scaled appropriately and representative of the levels expected from these tissues.

The expected Rayleigh behavior of the simulated speckle was verified by analysis of the population statistics. The measured BSC was normalized at each frequency by one half the mean value at that frequency $\overline{\eta}_{bs}(f)/2$ and the square root was taken. This normalization scales each BSC value so that the distribution for the square root is expected to be Rayleigh with scale parameter $\alpha = 1$. A histogram (Fig 8) shows that the resulting distribution, aggregated over all 1000 instances and all frequency bins, matches closely with the desired statistics.

2.4 Examples

A key result of quantitative simulation of ultrasound backscatter is the ability to create phantoms with realistic BSC spectra obtained directly from experimental data. We compiled BSC values measured experimentally by various authors for a number of useful tissues (see Figure 9). These are: normal and calcified human aortic wall (ex vivo) [6], human blood at 8% hematocrit (ex vivo) [9], human dermis and subcutaneous fat (in vivo) [7], and canine myocardium (ex vivo) [8]. Power-law functions were fitted to the data for the purpose of extrapolation, although in some cases other fit functions may be more appropriate. These curves can be combined together to create simulated phantoms composed of multiple tissues.

2.4.1 Imaging phantom for assessment of tissue detectability

As an example, we demonstrate an imaging phantom which can be used to assess the detectibility of various tissues for a given transducer design, reconstruction scheme, and noise model (see Fig. 10). This phantom is composed of cylindrical targets of three different sizes arranged by radius along the depth direction (top to bottom: 1.5 mm, 2.5 mm, and 3.5 mm) and by tissue along the axial direction (left to right: blood 8% hematocrit, normal aortic wall, canine myocardium, and calcified aortic wall). Each cylindrical target consists of randomly distributed targets with a number density of 20 targets/mm^3. RF data for each material was simulated separately using a 5 MHz 192-channel (150 μm pitch) elevation focused linear array, their corresponding filters applied in post-processing, and then recombined to form a single set of RF data.

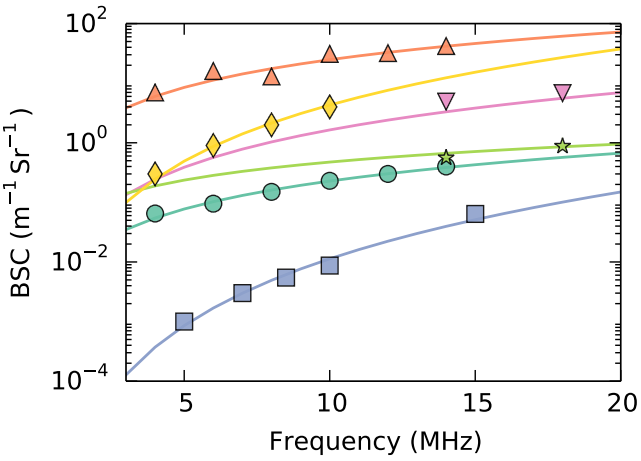

Figure 9: Backscattering coefficient spectra of different tissues measured experimentally by various authors (symbols) and their corresponding power-law fits (—). These curves can be used to design filters for simulation purposes. (Legend: calcified aortic wall (△) and normal aortic wall (◯) from Landini [6], subcutaneous fat (★) and dermis (▽) from Raju [7], canine myocardium from O'Donnell (♢) [8], and blood at 8% hematocrit from Shung (□)) [9].

For the sake of demonstration, a simple noise model was employed. Gaussian white noise of a constant power was added to each channel, where the power was selected to give a peak-SNR of 10 dB in the first case, and −5 dB in the second case. This corresponds to noise power levels of −417 dBW and −432 dBW, respectively. These levels are artificially small because the simulation was not tied to a specific transducer model (e.g. for piezoelectric or capacitive devices). In a full simulation, realistic transducer and noise models should be employed to tie signal and noise levels to absolute scales, thereby negating the need to designate peak-SNR.

B-mode images were reconstructed for both cases using a full synthetic aperture scheme. The reconstructed images provide an indication of which tissues we would expect to be able to accurately image based on choices such as the beamformation scheme, transducer design, and operating frequency. Such an analysis would not be possible without a quantitative treatment of backscattering coefficient. The realism of this phantom can be further improved with the addition of attenuation, either through Field II's built-in model or through other simulation enhancements [31].

2.4.2 Heart phantom

In addition to imaging phantoms, the method presented here can also be used to enhance the realism of anatomical phantoms. As an example, we created an anatomical phantom to mimic a view of the heart from an ICE catheter (see Figure 11). The view, adapted from a real image [32], shows atrial septal tenting due to a transseptal needle during an ablation procedure. The contrast of the

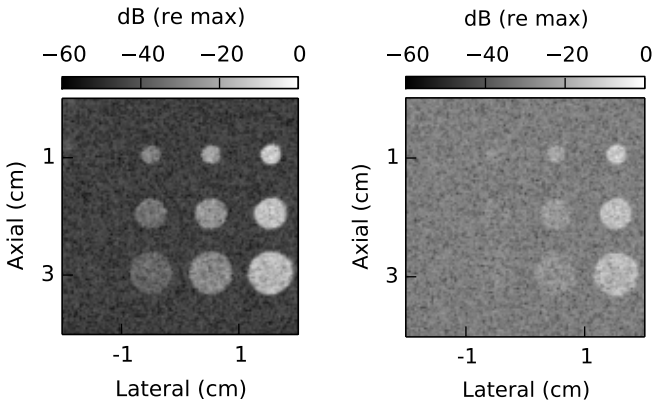

(a) (b)

Figure 10: Reconstructed images of a simulated phantom consisting of tissue-mimicking targets of varying backscattering coefficient (from left to right: blood at 8% hematocrit (not visible), normal aortic wall, canine myocardium, and calcified aortic wall). Different levels of Gaussian white noise were added to the simulated backscattered signal prior to beamformation: (a) -432 dBW noise power, (b) -417 dBW noise power. When combined with accurate noise and transducer transmit/receive models, this type of phantom can be used to assess a transducer's ability to detect specific tissues.

image is grounded quantitatively based on backscattering coefficient data for blood and myocardium. Furthermore, the variation of the contrast with respect to frequency, which may be significant for transducers with large bandwidth, is captured in a single simulation.

The heart phantom was generated by first populating a 3D domain with a random distribution of targets with a number density of 20 targets/mm^3 Next, each target was assigned to a material (blood and myocardium in this case) based on the projection of its position onto the imaging plane, where a 2D image served as a map. The method of using a 2D image as a reference can be extended to full volumetric phantoms, where the 2D image would be replaced with a full 3D anatomical model. RF data for each material was simulated separately using a 10 MHz 64-channel (63 μm pitch) 1D phased array, their corresponding filters applied in post-processing, and then recombined to form a single set of RF data. Finally, the B-mode image was reconstructed using a full synthetic aperture scheme.

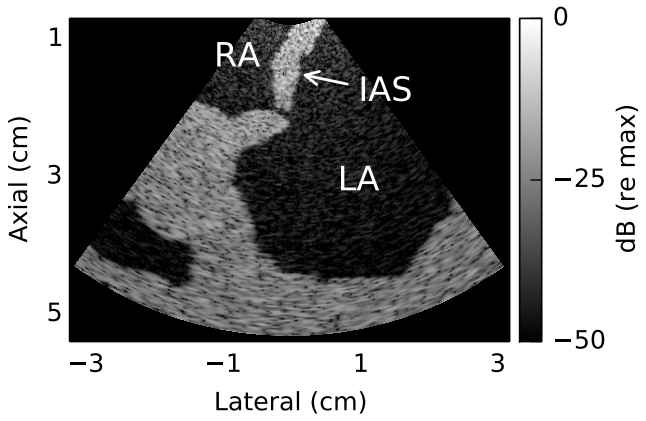

Figure 11: Reconstructed image using a 10 MHz ICE array of a simulated heart phantom with tissue backscattering coefficient matched to emprical data for blood and canine myocardium. (Legend: IAS, interatrial septum; RA, right atrium; LA, left atrium).

CHAPTER 3

FLOW IMAGING WITH ULTRASOUND

Doppler-based flow imaging has become an increasingly prominent tool for diagnosis of cardiovascular disease and for painting a clearer picture of the internal functions of the heart. Information on the magnitude and direction of blood flow in the heart can be used to detect and grade valvular regurgitation and other signs of disease. Unfortunately, technical limitations currently constrain the quality of flow images and their ability to accurately quantify the flow field. This is especially true for cardiac imaging because flow fields in the heart are complex and can contain a wide range of velocities. For these reasons, flow imaging is an intense area of research which can be aided significantly by the development of simulation tools.

In this chapter, we describe the development of simulation tools for flow imaging and demonstrate these tools by applying them to some simple problems. In Section 3.1, an overview of one-dimensional flow reconstruction algorithms and their advantages and disadvantages is presented. In Section3.2, we discuss multi-dimensional flow reconstruction algorithms and their corresponding technical challenges. In Section3.3, we outline a method for the simulation of flow based on the linear systems model. Finally, these simulation tools are applied to tackle some simple problems in Section 3.4

3.1 One-dimensional flow reconstruction

The fundamental building blocks of pulsed ultrasound flow reconstruction are time-delay estimation algorithms. Consider a succession of pulse-echo events where the echo signals received by the transducer are saved for processing. These signals form snapshots of the imaging medium, where motion in the medium will potentially manifest as delays in arrival time. How the arrival delays correspond to motion in the medium depends on the spatial characteristics of the array and its operation.

In the simplest case, we can transmit and receive a short ultrasound pulse along narrow lines using transmit and receive beamforming to form an A-scan. By windowing the A-scans at different times, we can localize the echos to specific regions of interest (ROI) along them. Comparison of the signals from the same ROI over time provide an estimate of the position and thus velocity of the echos. The problem thus boils down to the estimation of time-delays between successive signals.

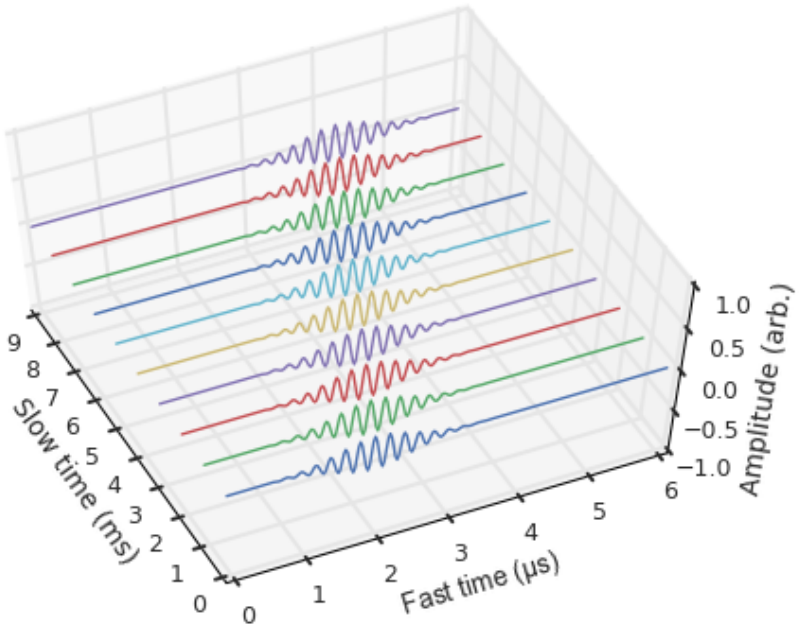

Figure 12: An example of a fast/slow-time matrix R for a single scatterer moving away from a transducer. The fast-time axis is sampled at f_s and the slow-time axis is sampled at f_{PRF}.

Time-delay estimation algorithms can be broadly categorized as either time-domain or frequency-domain methods. Here, we outline two time-domain methods–correlation lag and correlation search–and one frequency-domain method–instantaneous phase. For consistency, we adopt the following common notation.

Consider a set of time-sampled signals from successive pulse-echo events, where the pulse has a center frequency f_c. The signals are sampled at a sample frequency of f_s (corresponding to a sample period of T_s) and recorded at a pulse repetition frequency (PRF) of f_{PRF} (corresponding to a pulse repetition period of T_{PRF}. Let $R[i, k]$ represent the i-th sample of a time-sampled signal from the k-th frame (i.e. pulse-echo event). Then, R can be represented by a matrix, where the first dimension corresponds to the fast-time (sampled at f_s) and the second dimension corresponds to the slow-time (sampled at f_{PRF}).

3.1.1 Correlation lag algorithm

The idea behind time-domain algorithms is to estimate time delays using cross-correlation analysis. The simplest way to do this is to use the lag corresponding to the maximum of the cross-correlation between two signals [33]. This leads to the correlation lag algorithm.

Let $X(r_1, r_2, \tau)$ denote the normalized cross-correlation between two continuous-time signals r_1

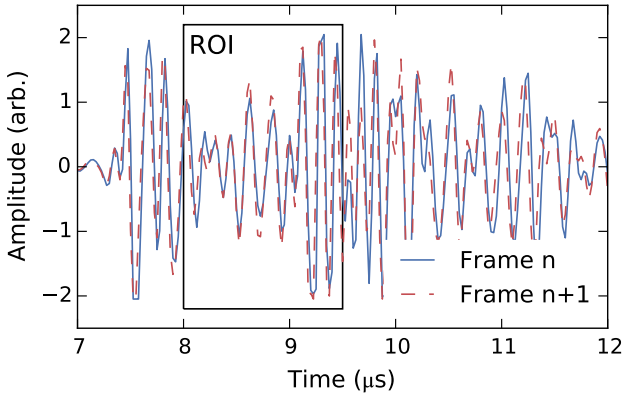

Figure 13: In the correlation lag algorithm, the signal from an ROI in one frame is correlated with the signal from the same ROI in the next frame. The time-delay is estimated from the lag corresponding to the maximum of the cross-correlation.

and r_2 at lags τ.

$$X(r_1, r_2, \tau) = \frac{\int_{-\infty}^{\infty} r_1(t) r_2(t+\tau)\,\mathrm{d}t}{\int_{-\infty}^{\infty} r_1(t) r_2(t)\,\mathrm{d}t} \tag{35}$$

Similarly, a discrete normalized cross-correlation can be defined for two time-sampled signals r_1 and r_2 at sample lags j. Zero-padding is used in the cases where the two signals do not overlap completely.

$$X(r_1, r_2, j) = \frac{\sum_{i=0}^{N-1} r_1[i] r_2[i+j]}{\sum_{i=0}^{N-1} r_1[i] r_2[i]} \tag{36}$$

We choose two signals from adjacent frames k and $k+1$. The argument of the maximum of the cross-correlation is multiplied by the sample period to get an estimate for the time delay between the two frames.

$$\begin{aligned} r_1[i] &= R[i, k] \\ r_2[i] &= R[i, k+1] \\ \Delta\tau_{est} &= T_s(argmax\,\{X(r_1, r_2, j)\}) \end{aligned} \tag{37}$$

The estimated time delay is related to position and thus the velocity of the medium in the ROI by the following expression.

$$v[k] = \frac{\left(\frac{c}{2} \cdot \Delta\tau_{est}\right)}{T_{PRF}} \tag{38}$$

The smallest resolvable velocity in (38) is limited by the sampling period T_s because this is the smallest lag calculated in the cross-correlation. Two methods are used in practice to improve the velocity resolution: (1) resampling of the time signals at a higher sampling rate, and (2) cubic

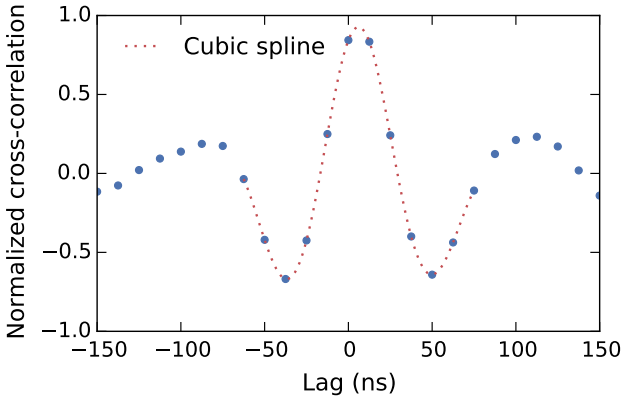

Figure 14: An example of a cross-correlation between two signals used in the correlation lag algorithm. Cubic spline interpolation is used to improve the resolution of the time lag corresponding to the maximum cross-correlation.

spline interpolation for estimating the peak correlation and its corresponding lag. It is also possible to improve the velocity resolution using frame interleaving, i.e. using non-adjacent frames in the cross-correlation. The largest resolvable velocity is limited by the length of the signals which is directly related to the size of the ROI.

3.1.2 Correlation search algorithm

It is possible to use the maximum correlation value as an estimate of the coherence of two signals [33]. This idea can be used for motion analysis by using the cross-correlation to compare a signal from one ROI to signals from nearby ROIs in subsequent frames. This approach leads is the basis of the correlation search algorithm.

As before, we choose two time-sampled signals r_1 and r_2 from adjacent frames.

$$r_1[i] = R[i, k]$$
$$r_2[i] = R[i, k+1]$$

The original signals are then divided into W windowed sections of some fixed width corresponding to a time duration T_w. These windows are spaced evenly over time, may overlap if desired, and in total will span the original signal length. We denote by $r_1|0$ the first windowed signal from r_1, $r_1|1$ the second windowed signal, etc. Let w_c represent the center window, where it is assumed that W

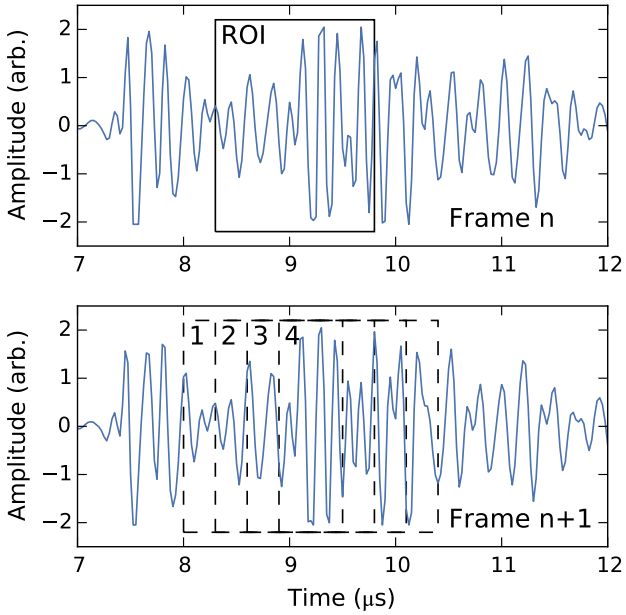

Figure 15: In the correlation search algorithm, the signal from the ROI in one frame is correlated with signals from several nearby ROIs from the next frame. The algorithm determines the time-delay corresponding to the maximum correlation coefficient using cubic spline interpolation.

is odd so that the center window is unambiguous.

$$r_1|w_1 \text{ for } w_1 = 0...(W-1)$$

$$r_2|w_2 \text{ for } w_2 = 0...(W-1)$$

$$w_c = (W-1)/2$$

Cross-correlations are calculated between the center window of signal 1 $r_1|w_c$, and all the windowed signals of signal 2 $r_2|w_2$. The maximum value of these cross-correlations is stored in a vector m. Cubic splines are used to interpolate the m and determine the peak correlation and its corresponding argument.

$$m[w_2] = max\left\{X(r_1|w_c, r_2|w_2, j)\right\} \text{ for } w_2 = 0...(W-1) \tag{39}$$

From this we can obtain an estimate of the time delay and thus an estimate of the velocity.

$$\Delta\tau_{est} = \Delta T_w(w_c - argmax\left\{x[w_2]\right\}) \tag{40}$$

$$v[k] = \frac{\left(\frac{c}{2} \cdot \Delta\tau_{est}\right)}{T_{PRF}} \tag{41}$$

3.1.3 Instantaneous phase algorithm

A number of frequency-domain time-delay estimation algorithms have been introduced in the literature. The most successful of these is an algorithm based on instantaneous phase (also called the one-dimensional autocorrelator) [34].

In order to do processing based on frequency-domain methods, the signals must first be converted to their analytic representation. This can be done using the Hilbert transform, but for the sake of efficiency, IQ (in phase-quadrature) demodulation of the signals is preferred since these can be readily implemented in electronics. In IQ demodulation, the signals are mixed with sines and cosines of the center frequency of the signal, low-pass filtered, and then down-sampled accordingly. These operations are performed along the fast-time axis of the signals and repeated for every frame, resulting in two matrices $I[i,k]$ and $Q[i,k]$.

$$\begin{aligned} I[i,k] &: \text{in phase component} \\ Q[i,k] &: \text{quadrature component} \\ R[i,k] &= Re\left[(I[i,k] + jQ[i,k])exp(j2\pi f_c i T_s)\right] \end{aligned} \tag{42}$$

The goal of the instantaneous phase method is to estimate the instantaneous frequency along the slow-time dimension by estimating the derivative of the phase using a finite difference (ideally with as few frames as possible).

$$\omega = \frac{d\phi}{dt} \approx \frac{\phi[i,k+1] - \phi[i,k]}{T_{PRF}} \tag{43}$$

To relate this to IQ demodulated signals, note the following equivalence which can be derived from trigonometric identities.

$$tan(\phi[i,k+1] - \phi[i,k]) = \frac{sin(\phi[i,k+1] - \phi[i,k])}{cos(\phi[i,k+1] - \phi[i,k])} \tag{44}$$

$$= \frac{sin(\phi[i,k+1])cos(\phi[i,k]) - cos(\phi[i,k+1])sin(\phi[i,k])}{cos(\phi[i,k+1])cos(\phi[i,k]) - sin(\phi[i,k+1])sin(\phi[i,k])} \tag{45}$$

Replacing the sines and cosines with in-phase and quadrature components and combining with (43) yields an expression for the estimated instantaneous frequency. Averaging is performed over several

frames (the length of which is referred to as the ensemble length N_{ens} improves the estimate.

$$\overline{\omega}[i,k] = \frac{1}{T_{PRF}} arctan\left[\frac{\sum_{j=k}^{N_{ens}} Q[i,j+1]I[i,j] - I[i,j+1]Q[i,j]}{\sum_{j=k}^{N_{ens}} I[i,j+1]I[i,j] - Q[i,j+1]Q[i,j]}\right] \tag{46}$$

Finally, the instantaneous frequency is related ot the velocity of the medium by the following:

$$v[i,k] = \frac{c}{2}\left(\frac{\overline{\omega}[i,k]}{\omega_c}\right) \tag{47}$$

While there is no lower bound imposed by the instantaneous phase method on the minimum resolvable velocity (barring practical constraints), there is a hard upper bound on the largest measurable velocity. This can be understood as a consequence of the Nyquist sampling theorem, since we are sampling the signal along the slow-time axis at a rate f_{PRF}. The largest representable frequency before aliasing occurs is $f_{PRF}/2$, which corresponds to the following velocity:

$$v_{upper} = \frac{c}{2}\left(\frac{\omega_{PRF}/2}{\omega_c}\right) \tag{48}$$

3.1.4 Discussion

Of the three algorithms described here–correlation lag, correlation search, and instantaneous phase–the instantaneous phase algorithm is the most widely used and can be found in most commercial ultrasound systems (usually under the name color flow or pulse doppler). Its preference over other algorithms is due to its ease of implementation (especially with IQ data) and its computational efficiency. The time-domain algorithms, relying on the calculation of cross-correlations and spline interpolation, are more difficult computationally, although the increased computation costs are not generally prohibitive.

The time-domain methods, however, do hold some advantages over the instantaneous phase method [33]. When used on raw data (no extra processing or averaging), the time-domain methods tend to be more precise and perform better in noisy environments. Time-domain methods also do not suffer from an aliasing limit; their largest measurable velocity depends only on the size of the ROI/search area and on sources of decorrelation. Finally, in time-domain methods, increasing the bandwidth of the pulse improves both the precision of the correlation analysis and the spatial resolution of the image. In the instantaneous phase method, increased bandwidth of the pulse results in velocity dispersion and ambiguity in the velocity estimate due to the presence of more

frequencies. Narrow-band pulses are therefore desirable and this leads to an inherent trade-off between pulse bandwidth and spatial resolution.

All three of these estimation techniques can be improved using various types of averaging. Averaging can be performed over multiple frames to improve SNR but at the expense of smoothing out motion in the medium. Spatial averaging can also be used after estimates are obtained which will result in some smoothing of the spatial variation of the motion in the medium.

3.2 Multi-dimensional flow reconstruction

It has been shown that motion can be detected by ultrasound arrays by estimating time delays between successive pulse-echo events. This technique, however, can only capture the motion along the direction of wave propagation, since motion perpendicular to the propagating wave will not result in changes in arrival time. This is a well-known limitation of doppler methods which limits modern clinical systems to showing only the projection of the real flow field along the axis aligned away from the transducer. In specific cases where the blood flow is constrained primarily to one direction, e.g. arterial blood flow, the orientation angle of the transducer with respect to the expected flow direction can be used as a correction on the measured velocities. However, in many cases of clinical interest, such as flow through arterial bifurcations, around vascular occlusions and in the interior of the heart, the nature of the blood flow is much more complicated and the ability to reconstruct full three-dimensional flow fields is highly desirable.

A number of techniques to perform 2D/3D flow reconstruction have been explored in the literature. The first of these systems used continuous doppler with multiple transducers orientated at angles to create cross-beams [35]. This concept has been extended to pulsed doppler systems using single transducers but processing using different sub-apertures [36] [19]. The underlying working principle of all these techniques is identical: to exploit the spatial extent of the transducer aperture to obtain flow measurements along several different angles. By interrogating locations in the medium using different angles, an estimate of the flow magnitude and direction can be obtained. The reconstruction method for all these techniques can be unified in a mathematical formulation using linear algebra [37].

Consider a vector flow field with velocity $\vec{v}(x, y, z, t)$ defined as a function of space and time. This field is interrogated at a position $\vec{r}$ by an array with transmit element located at $\vec{r}_{tx}$ and receive element located at $\vec{r}_{rx}$. From a ray perspective, the ultrasound pulse can be considered to travel towards the observation point in the direction of the unit vector $\vec{i}_{tx}$ and to return towards the

transducer along the unit vector $-\vec{i}_{rx}$, where the vectors are defined as:

$$\vec{i}_{tx} = \frac{\vec{r} - \vec{r}_{tx}}{|\vec{r} - \vec{r}_{tx}|} \tag{49}$$

$$\vec{i}_{rx} = \frac{\vec{r} - \vec{r}_{rx}}{|\vec{r} - \vec{r}_{rx}|} \tag{50}$$

The speed s measured along this path due to the flow field will have equal contributions from the projection of the flow vector onto vectors $\vec{i}_{tx}$ and $-\vec{i}_{rx}$.

$$s = \frac{1}{2}(\vec{v} \cdot \vec{i}_{tx}) + \frac{1}{2}(\vec{v} \cdot \vec{i}_{rx}) \tag{51}$$

Consider now the speed measured simultaneously using N different receive elements separated in space. The resulting linear system of equations can be used to solve for the three orthogonal components of the flow field.

$$\begin{pmatrix} i_{0,x} + i_{tx,x} & i_{0,y} + i_{tx,x} & i_{0,z} + i_{tx,x} \\ i_{1,x} + i_{tx,x} & i_{1,y} + i_{tx,x} & i_{1,z} + i_{tx,x} \\ \vdots & \vdots & \vdots \\ i_{N-1,x} + i_{tx,x} & i_{N-1,y} + i_{tx,x} & i_{N-1,z} + i_{tx,x} \end{pmatrix} \begin{pmatrix} v_x \\ v_y \\ v_z \end{pmatrix} = \begin{pmatrix} s_0 \\ s_1 \\ \vdots \\ s_{N-1} \end{pmatrix}$$

If $N > 3$ the problem is over-constrained and a solution can be found that minimizes the error in a least-squares sense. The accuracy of the reconstruction will depend significantly on the quality of the vector projections (quality in the sense that the vectors adequately spans $\mathbb{R}^3$). The problem can be further constrained by including different forms of regularization, for example regularizing based on expected properties of the flow field [37].

Note that the mathematical formulation presented here is fairly flexible; the notion of transmit and receive elements used here need not represent actual elements of the array, but may instead represent sub-apertures of an array that are focused in arbitrary directions. In this situation, the directions used should correspond to the ray-path between the observation point and the center of the sub-apertures.

While vector projection based reconstruction is the most natural extension of one-dimensional reconstruction algorithms to two and three dimensions, it is not the only method that has been

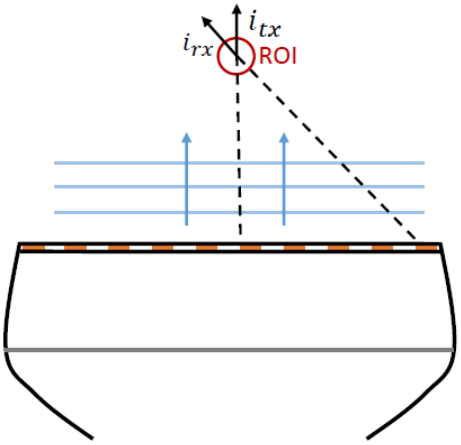

Figure 16: The problem geometry for multi-dimensional flow reconstruction using ultrasound. The direction of the transmitted wave at the ROI determined the vector i_{tx} and the direction from the ROI to the receiving element determines i_{rx}. The motion of the medium in the ROI is projected onto these two vectors.

explored. Other suggested solutions include 2D/3D cross-correlation analysis on beamformed images [38] [19], and more recently introducing lateral sensitivity based on spatial quadrature (also called transverse oscillation) [39] [40].

3.2.1 Beamforming schemes for flow reconstruction

The flow reconstruction method used should be considered in conjunction with a suitable beamforming scheme since their operations are intimately intertwined. In flow imaging, the speed at which images are acquired is of critical importance to the performance of the reconstruction. For example, consider the traditional beamforming scheme for B-mode where the image is formed line by line by focusing in both transmit and receive operation. The reconstruction of an image will require multiple firings in order to span the entire imaging domain. For 2D images, the number of firings required can be around 256, while for 3D volumetric images the required number of firings jumps to 3600 (for a 60° by 60° FOV with 1° line density). Because flow reconstruction depends on comparison of the same ROI over time, the large number of firings, by virtue of increasing the time between comparisons, will degrade the quality of the reconstruction.

A number of solutions to reduce the number of firings needed have been explored in the literature. One solution with particular promise is Ultrafast ultrasound imaging [41] which is based on the principle of synthetic aperture beamforming. In synthetic aperture beamforming, diverging pulses are transmitted into the medium and the backscattered signals are recorded simultaneously on all receive elements. Beamforming of the received signals is performed using software, allowing for all

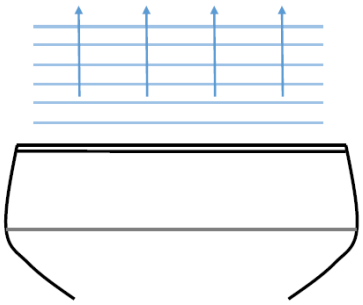

Figure 17: In plane wave transmit mode, all elements of the transducer are excited at the same time, producing a traveling wave with an approximately planar wave front. Plane wave transmit mode sends energy into a larger region at the expense of transmitted pressure amplitude and SNR.

possible delays to be applied simultaneously and producing an entire image, albeit of low resolution, from a single firing. These low resolution images are then improved successively using either firings from the same transmit pulse (akin to averaging) or firings from transmitted pulses originating from different locations of the array (synthetic transmit aperture). Flow reconstruction benefits from Ultrafast techniques because flow estimates can be performed on the low quality images (obtained very quickly) and then improved using successive estimates. Further improvements to SNR can be obtained using spatially-coded excitations in combination with orthogonal temporal coding [42] [43].

3.3 Simulating ultrasonic backscatter from blood flow

The methods outlined in Chapter 2 can be extended to include the simulation of flowing media. In Chapter 2, it was suggested that tissue be represented in simulation using equivalent scattering distributions with properties based on experimental characterization of various tissues. To simulate motion, these scatterer positions can be incremented in time by advancing along their predicted trajectories. Consider a known continuous vector-valued function F which describes the velocity at position $\vec{r} = \langle r_x, r_y, r_z \rangle$ and time t.

$$\vec{v} = \frac{\partial \vec{r}}{\partial t} = F(\vec{r}, t) \tag{52}$$

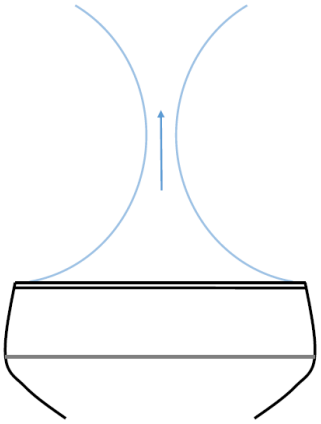

Figure 18: In focused transmit mode, each element of the transducer is phased to provide maximum pressure output at a specific point in space. This maximizes SNR but requires several pulse-echo events to interrogate the imaging domain.

This leads to the following set of coupled ordinary differential equation which can be solved numerically using standard ODE solvers.

$$\begin{aligned} \frac{\partial r_x}{\partial t} &= F(\vec{r}, t) \cdot \vec{x} \\ \frac{\partial r_y}{\partial t} &= F(\vec{r}, t) \cdot \vec{y} \\ \frac{\partial r_z}{\partial t} &= F(\vec{r}, t) \cdot \vec{z} \end{aligned} \tag{53}$$

With this simulation method, special care should be made to ensure that the flow field is divergence-free (incompressible), otherwise the assumption of uniform scattering distribution for the Rayleigh speckle model may be violated.

With the addition of flow capabilities, we now have a framework for the comprehensive simulation of pulse-echo ultrasound from transducers. In this framework, we can simulate the entire imaging process, capturing important effects such as diffraction from weighted and phased transducer arrays; backscatter and attenuation from different types of tissue; tissue motion; and choices related to beamforming, signal processing, and image reconstruction. This framework can be used as a tool to examine the efficacy of different transducer designs or investigate the effect specific changes may have on the overall system performance.

As an example, consider the simulation of a potential flow imaging setup. The conceptual flow of data in the simulation and relationships between the various models are depicted in Figure 19. In the next section, we implement this simulation and provide some examples of how it can be used.

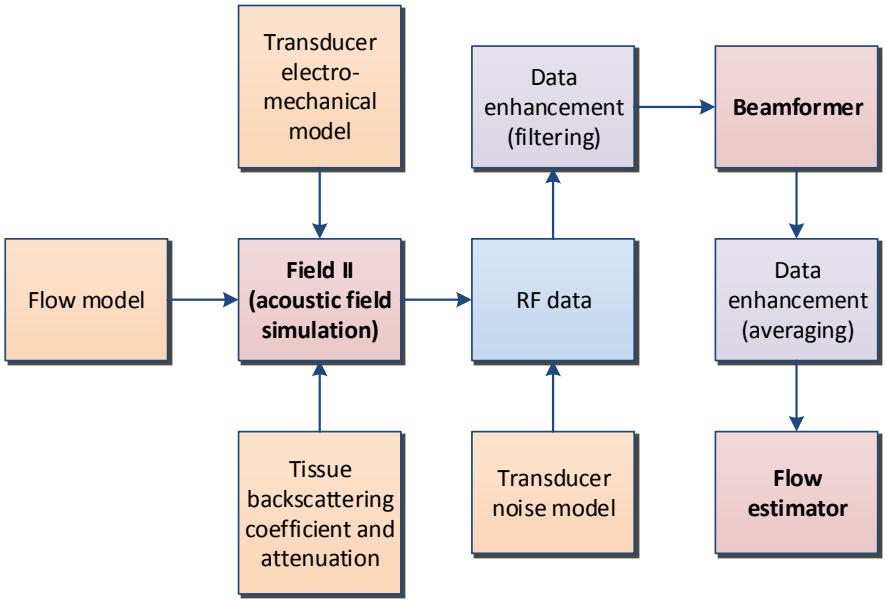

Figure 19: Flow chart for the proposed flow simulation method showing the relationships between the various models.

3.4 Examples

3.4.1 Assessing performance of one-dimensional reconstruction algorithms using experimental data

For our first example, we assessed the efficacy of the one-dimensional flow reconstruction algorithms (described in Section 3.1) using pre-beamformed RF data obtained experimentally. In this experimental setup, a styrofoam target was attached to a mechanical shaker (B&K Measurement Exciter Type 4810) and submerged in a water bath. A 128-element linear ultrasound probe (Ultrasonix L14-5/38) and ultrasound system (Ultrasonix SonixTOUCH) were used to transmit and receive ultrasound pulses. The probe was oriented such that the motion of the styrofoam target is along the primary axis of the transducer. The ultrasound system was programmed to transmit focused pulses at a center frequency of 6.6 MHz and at a pulse repetition frequency of 2 kHz while the shaker is excited with 5 cycles of a 15 Hz sine. In addition, a laser doppler vibrometer (LDV, Polytec IVS-400) was used to measure the velocity of the styrofoam target for the purpose of comparison.

The raw echo signals were recorded on all 128 channels simultaneously using an Ultrasonix SonixDAQ. An example of an A-scan from the styrofoam target (see Figure 20) shows the speckle-like behavior of the backscatter. These echo signals were then beamformed using synthetic receive aperture and processed using one of the three one-dimensional flow algorithms (correlation lag, corre-

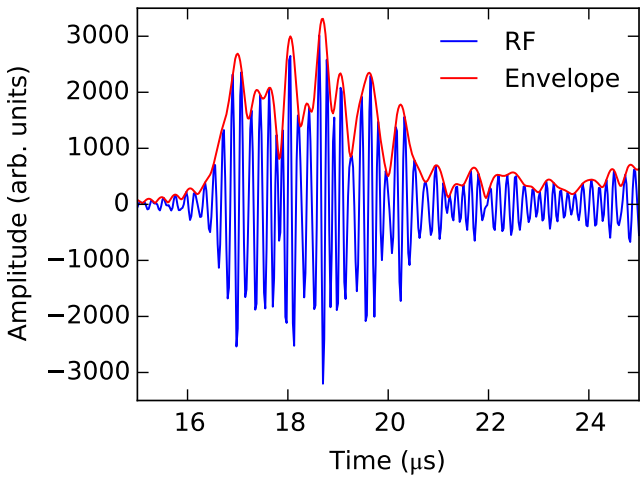

Figure 20: Backscattered RF signal from a styrofoam target exhibiting speckle-like interference.

lation search, and instantaneous phase). For a fair comparison, we considered only the performance of the frame-to-frame estimate (no averaging).

The estimated velocities are shown compared with the LDV output in Figure 21. We see that overall the performance of all three algorithms was sufficient to track the motion of the target. The correlation lag seems to be the best performer under these conditions, producing the most consistent and precise estimate, especially during times where the velocity changes direction. The correlation search and instantaneous phase algorithms suffer from spike artifacts which may be reduced by averaging.

In addition, to compare the noise performance of the different algorithms, gaussian white noise was artificially added to the pre-beamformed RF data to produce signals with SNR of 5, 10, and 20 dB. These noise-added signals were then used in reconstruction and the error was calculated using the LDV measurements as a reference case. The standard deviation of the error for each algorithm is shown in Figure 22. The correlation lag algorithm produced the most accurate estimates in the presence of noise, followed by the correlation search algorithm and finally the instantaneous phase algorithm.

3.4.2 Assessing performance of three-dimensional reconstruction algorithms using simulated data

For our second example, we conducted a pure simulation study of the multi-dimensional reconstruction algorithm described in Section 3.2 for reconstruction of three-dimensional flow. In Field II, RF data was simulated for a 128 element 300 μm pitch linear array with a center frequency of 5

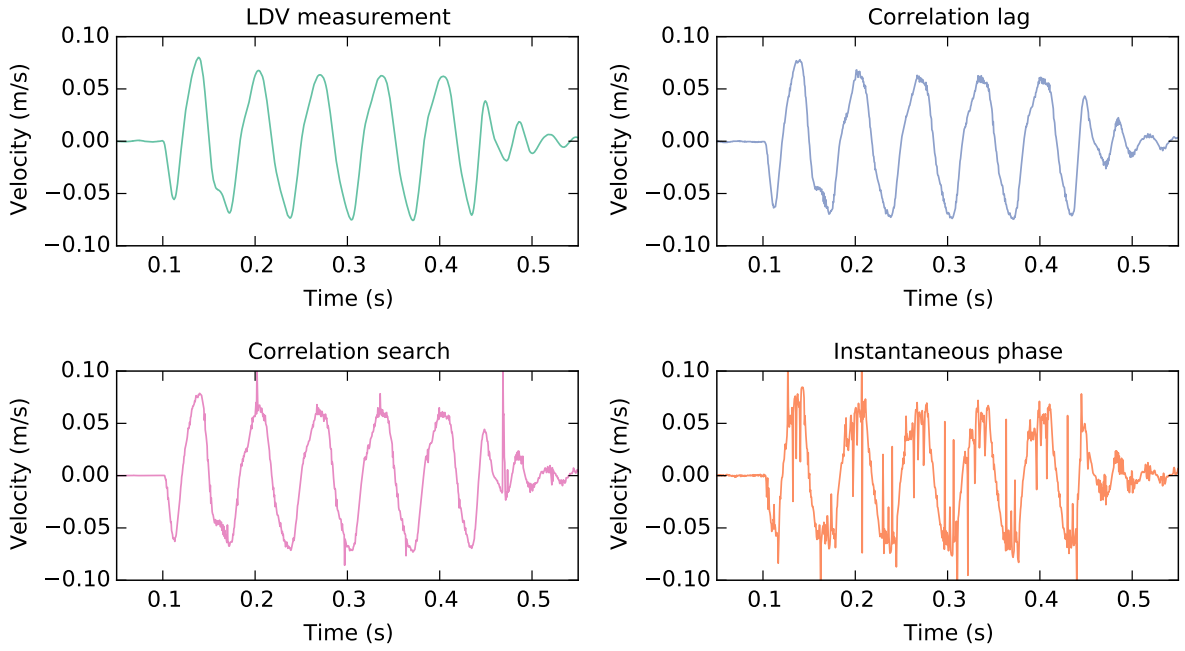

Figure 21: Comparison of the different velocity estimation algorithms with LDV measurement for reference. The estimates were performed using only frame-to-frame information (no averaging) to maintain a fair comparison.

MHz. Pulse-echo images were obtained using plane wave transmit and synthetic receive aperture at a pulse reptition frequency of 1 kHz. The simulated blood was composed of randomly-distributed scatterers with a number density of 20scatterers/mm^3 and BSC based on blood at a hematocrit of 8% [9]. Full 3D volumetric flow estimates were obtained using the correlation lag algorithm with $2x$ resampling. Vector estimates were performed using the inversion method described in Section 3.2 with the left-most and right-most sub-apertures of the array, both with 8 elements each.

We considered three different flow fields of increasing complexity. First, we simulated a flow field with constant x and z components (referred herein as the xz flow field). Defining the z axis normal to the face of the array (axial direction), x along the length of the array (lateral direction), and y perpendicular to x and z (elevation direction), the flow field is defined as:

$$v_x = \langle 0.01, 0, 0.01 \rangle \,\mathrm{m/s} \tag{54}$$

$$|\vec{v}| \approx 0.01414\,\mathrm{m/s}$$

Second, we simulated the same flow with the addition of a y component (referred herein as the xyz

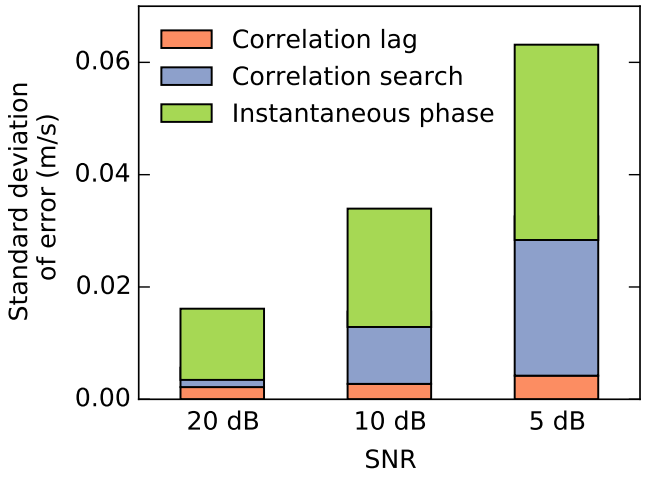

Figure 22: Noise performance characterized by the standard deviation of the error for the different velocity estimation algorithms. Gaussian white noise was added to RF signals to simulate different SNR conditions.

flow field).

$$v_x = \langle 0.01, 0.01, 0.01 \rangle \,\mathrm{m/s} \tag{55}$$
$$|\vec{v}| \approx 0.01732 \,\mathrm{m/s}$$

Third, a vortical flow field was simulated with rigid-body rotation in the x-y plane and a constant z component (referred herein as the rotating flow field). Defining the cylindrical coordinates $r \equiv \sqrt{x^2 + y^2}$ and $\theta \equiv tan^{-1}(y/x)$, the flow field is given by

$$\omega = 1.33 \,\mathrm{rad/s} \tag{56}$$
$$v_x = \langle \omega r sin\theta, \omega r cos\theta, 0.01 \rangle \,\mathrm{m/s}$$
$$|\vec{v}| = \sqrt{(\omega r)^2 + 0.01^2} \,\mathrm{m/s}$$

These three flow fields are shown in Figure 26, Figure 28, and Figure 30, and their reconstructed fields shown in Figure 27, Figure 29, and Figure 31.

Because the array lies along the x direction, it is expected that the reconstructed fields will have spatial discriminability in only the x and z direction, i.e. the reconstructed field will be the projection of the actual field onto the x-z plane. Furthermore, the constant nature of the xz and xyz flow fields should make for a relatively straight-forward reconstruction. The error statistics (mean and standard deviation) for each component of the reconstructed fields are shown in Table 1. The error

flow field	**x (mm/s)**		**y (mm/s)**		**z (mm/s)**	
	mean	std	mean	std	mean	std
xz	-0.42	0.73	-7.0×10^{-17}	1.2	-0.13	0.24
xyz	-0.38	0.73	-10	0.12	-0.13	0.26
rotating	-5.1×10^{-2}	8.1	-2.3×10^{-15}	8.2	-0.12	0.21

Table 1: Mean and standard deviation of the error for the three components of the reconstructed flows.

distributions for these reconstructions are shown in Figure 23, Figure 24, and Figure 25.

Referring to the first two reconstructed fields and their error statistics, we see that the behavior of the reconstructed *xz* and *xyz* fields match our intuition. The *xz* flow field is reconstructed faithfully with the standard deviation of the error less than 1 mm/s in both x and z directions. The *xyz* field is reconstructed with similar low error in the x and z directions, but with a y direction estimate that provides no reliable information about the flow field.

The reconstructed rotating flow field behaves unexpectedly. The z component of the reconstructed field is reproduced accurately with less than 1 mm/s standard deviation in the error. However, both the x component and y components of the reconstructed fields have very large error and are completely unreliable. This indicates that the introduction of a more complicated flow in the x-z plane has completely destroyed the x-directed spatial discriminability of the array and of the reconstruction algorithm. While it is not abundantly clear why this occurs, it is hypothesized that the poor lateral resolution and significant side-lobes of the array may allow off-axis signals to corrupt the correlation analysis used for reconstruction. If this is indeed the case, the problem may be ameliorated with aggressive apodization and the use of beamforming schemes with better lateral resolution.

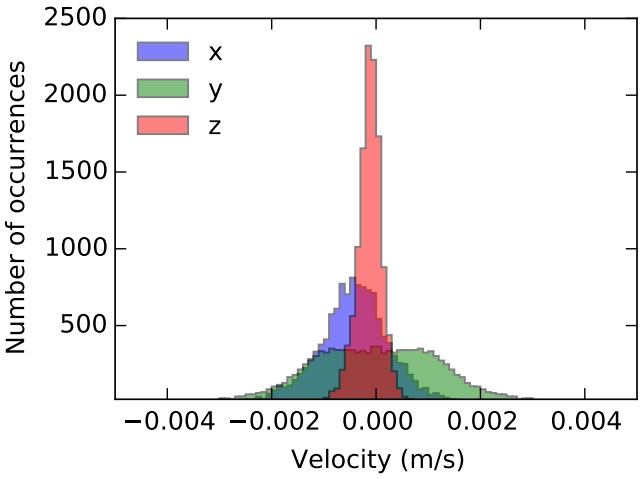

Figure 23: Error distributions for the three components of the reconstructed constant x and z flow field.

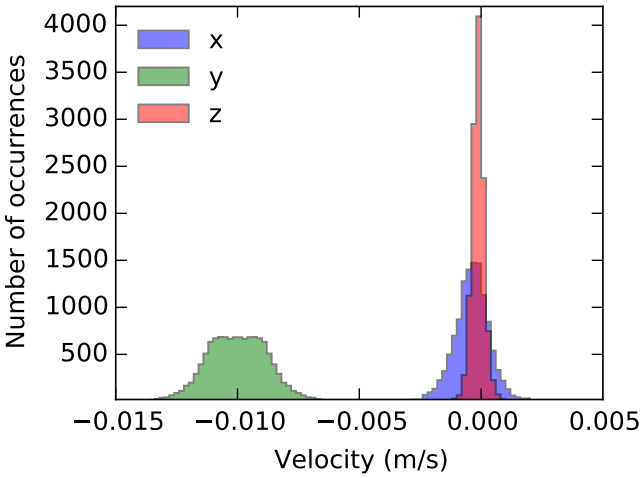

Figure 24: Error distributions for the three components of the reconstructed constant x, y, and z flow field.

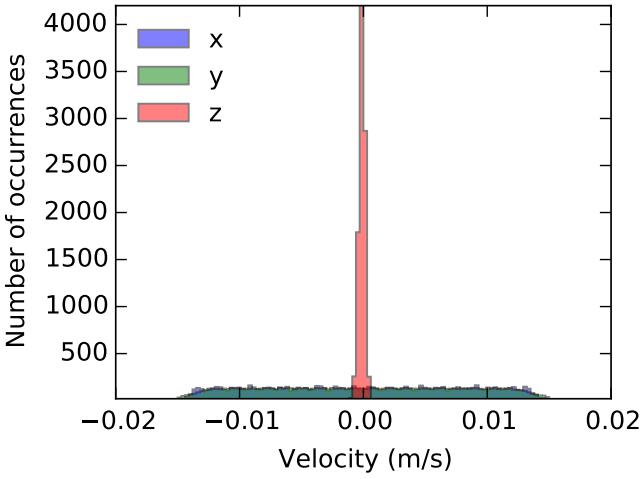

Figure 25: Error distributions for the three components of the reconstructed rotating flow field.

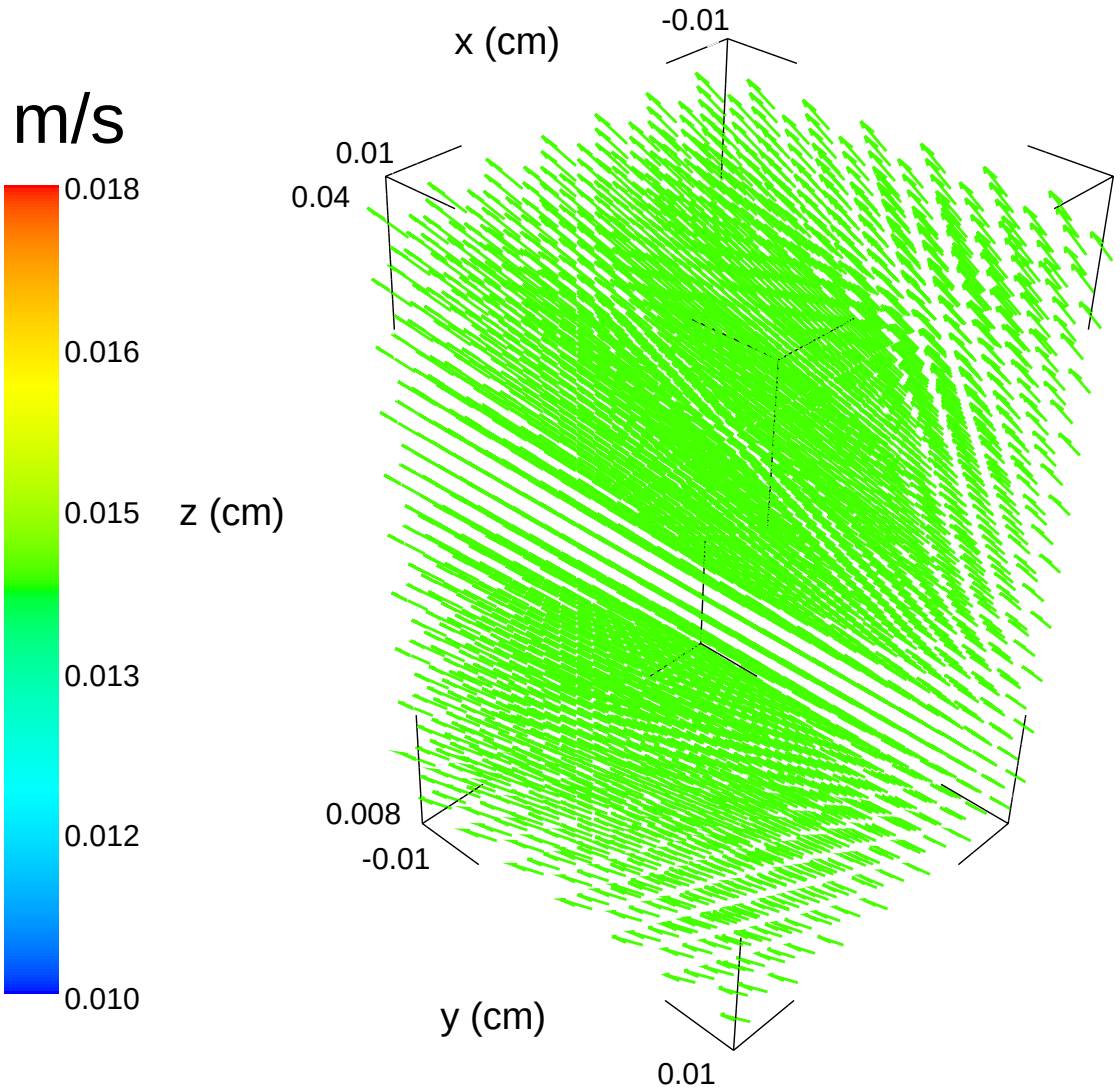

Figure 26: Vector plot of the simulated flow field with constant x and z components of 0.01 m/s and no y component.

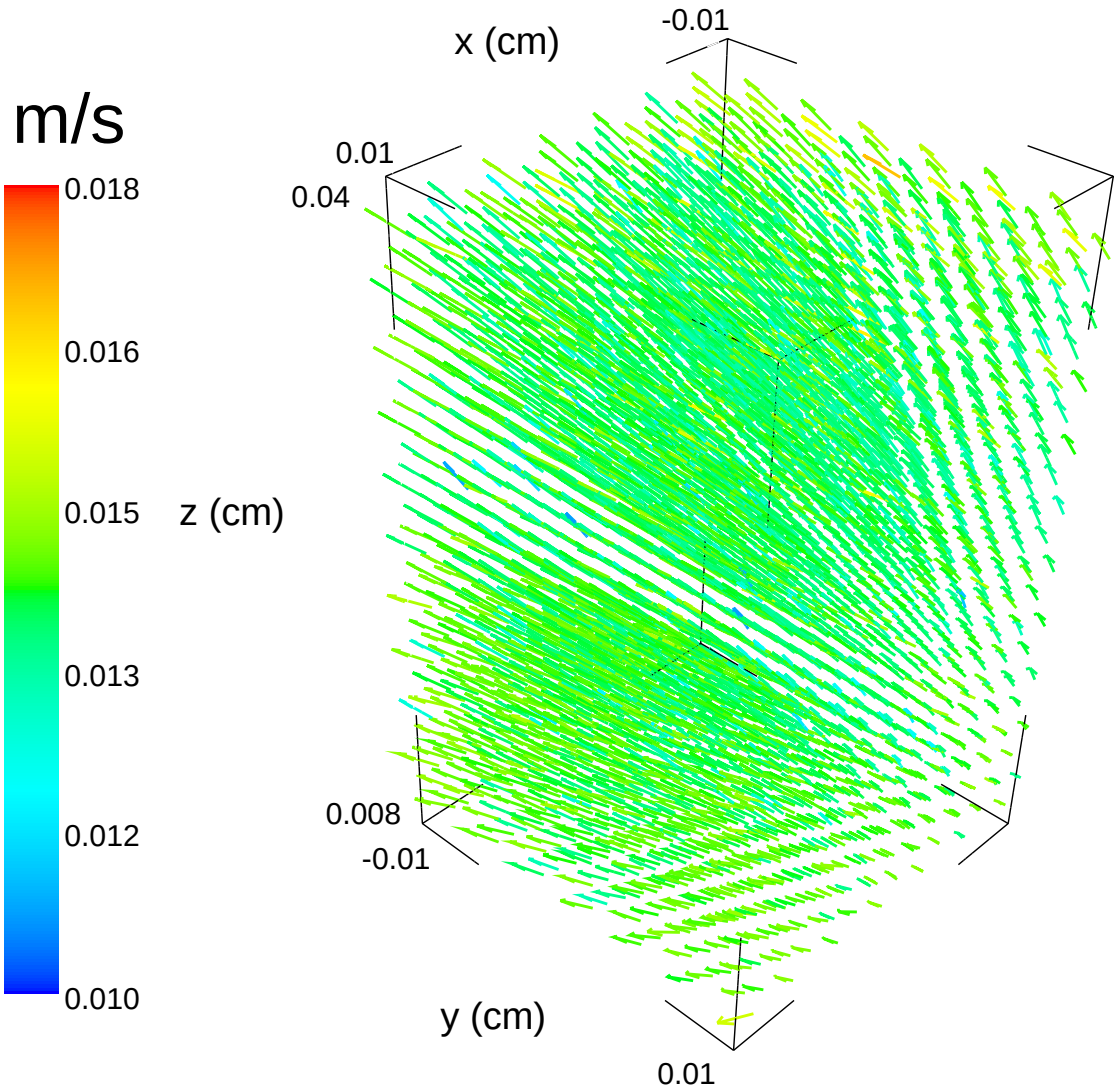

Figure 27: Vector plot of the reconstructed flow field with constant x and z components using a simulated 128-element linear array and the projection inversion technique.

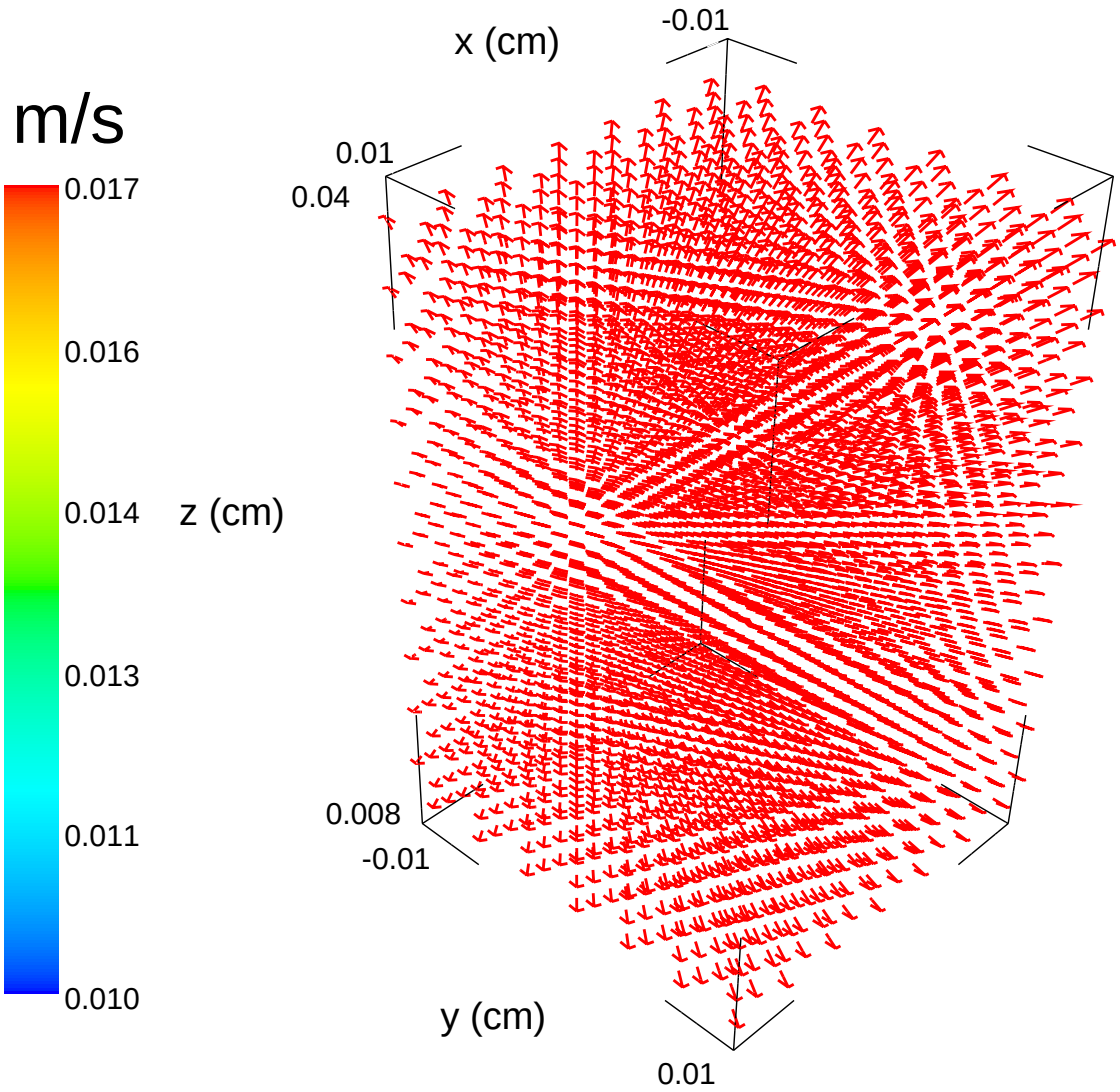

Figure 28: Vector plot of the simulated flow field with constant x, y, and z components of 0.01 m/s.

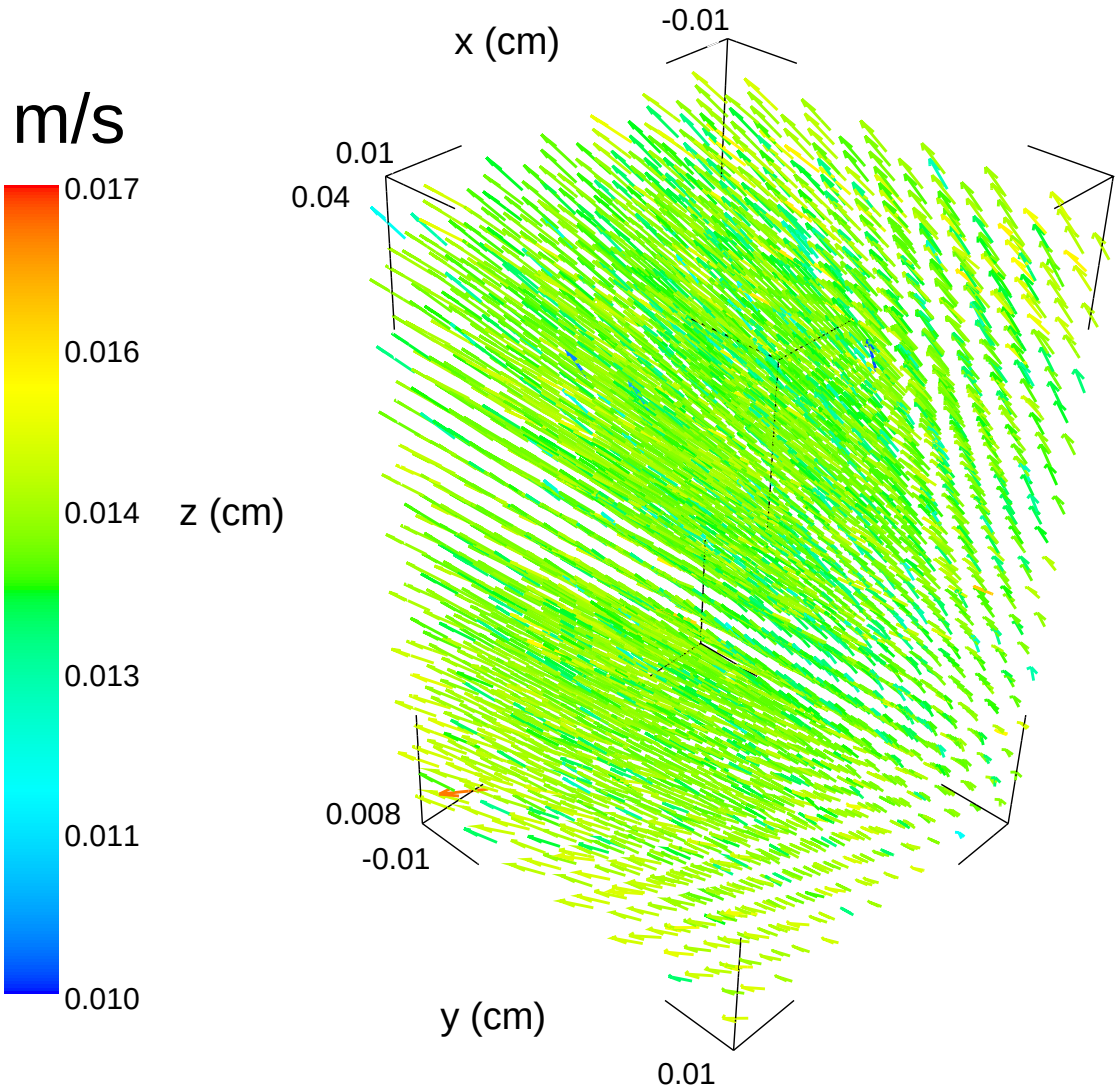

Figure 29: Vector plot of the reconstructed flow field with constant x, y, and z components using a simulated 128-element linear array and the projection inversion technique. The reconstruction is not able to capture the y-directed flow because the array has no spatial discriminability in the y direction.

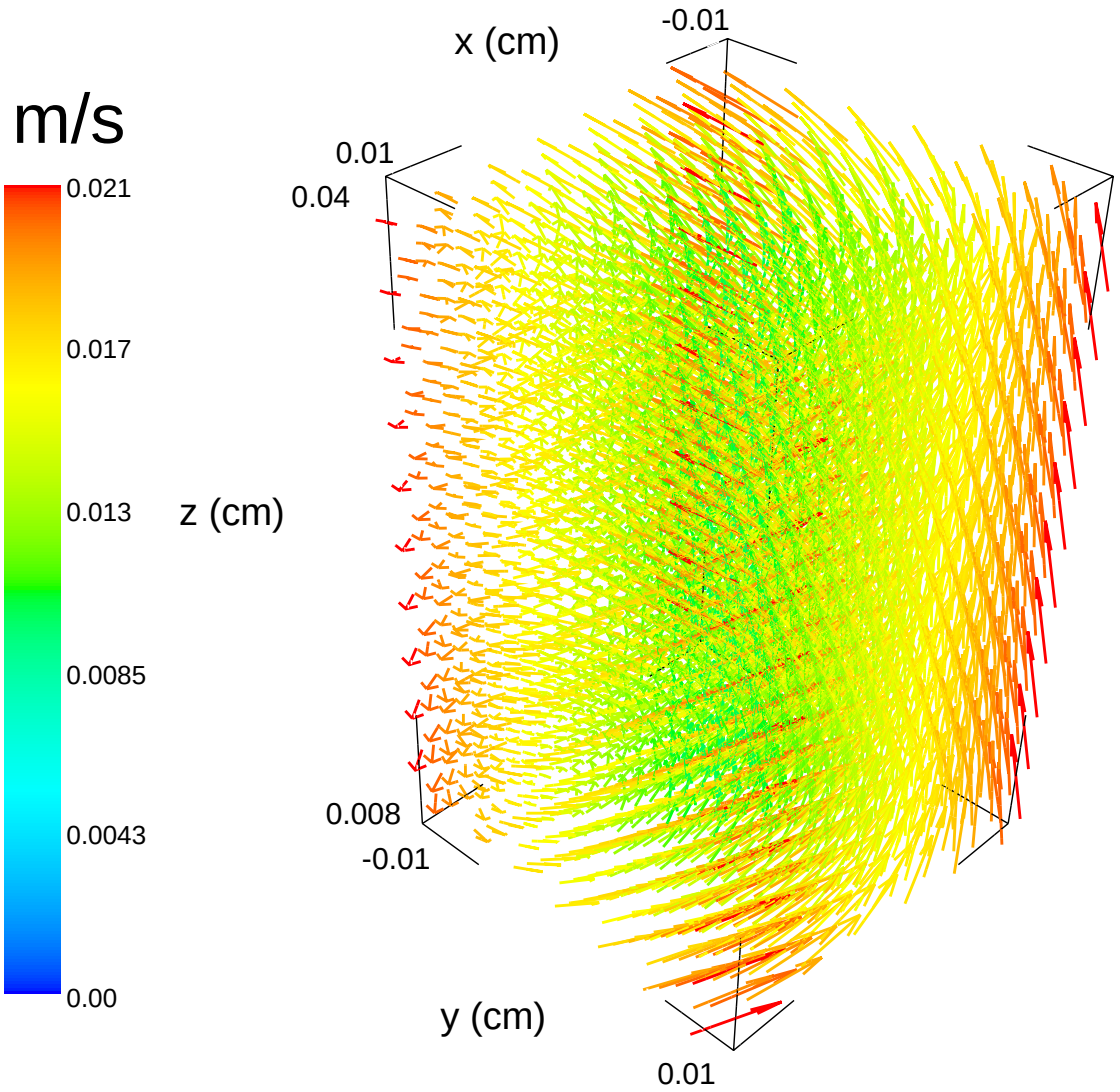

Figure 30: Vector plot of the simulated flow field with constant z component of 0.01 m/s and rigid body rotation in the x and y directions of 1.33 radians/s.

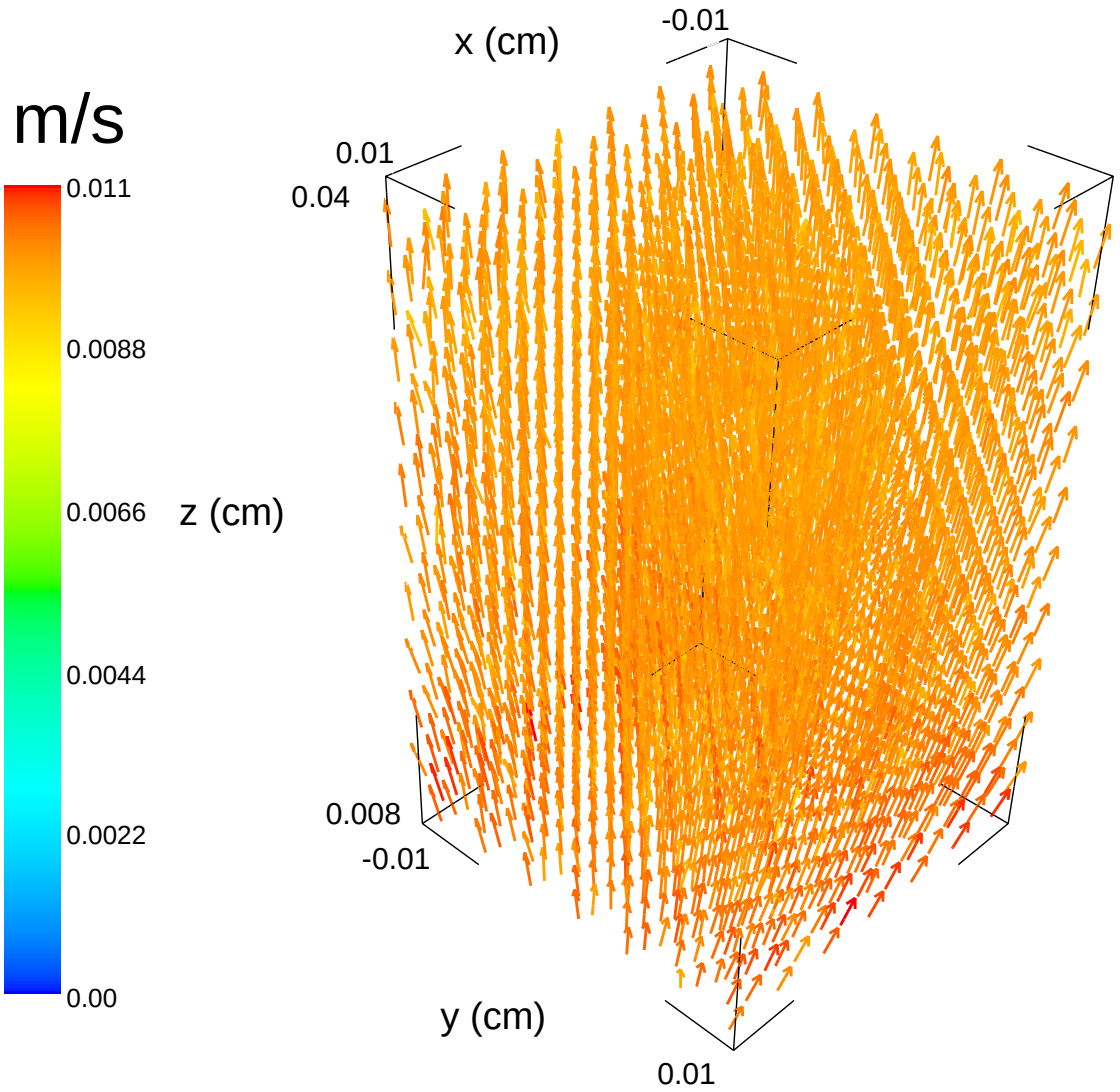

Figure 31: Vector plot of the reconstructed flow field with constant z component and rigid body rotation in the x and y directions using a simulated 128-element linear array and the projection inversion technique. The reconstruction is not able to capture the x-directed nor the y-directed flow.

CHAPTER 4

CONCLUSION AND FUTURE WORK

We have described the development of tools for the quantitative simulation of tissue backscatter and blood motion for ultrasonic transducers used in medical imaging. These tools, based on the linear systems model for acoustic fields from transducers, can be used to simulate the full chain of events necessary for the reconstruction of pulse-echo images, capturing important effects such as diffraction, lossy media, choice of beamforming scheme, and array design. Most significantly, we have extended these tools to include the realistic simulation of tissue backscatter through backscattering coefficient and the application of the Rayleigh model for tissue speckle.

We demonstrated through several examples how these simulation tools can be used to investigate a variety of problems. First, a simulated phantom was demonstrated which can be used to predict tissue detectiblity performance of transducers for various tissues such as blood, aorta, and myocardium. Second, a simulated phantom was created to mimmick the interior of the heart in order to present a realistic environment from which array designs can be tested. Third, experimental data was used to test common algorithms for one-dimensional doppler imaging. Fourth, RF data simulated for three simple flow fields was used to study three-dimensional flow reconstruction based on vector projection.

A number of natural extensions to this work have been left to future studies. The application of the Rayleigh model for speckle has confined the scope of our simulations to fully-developed speckle characteristic of diffuse tissue. Many tissues, however, are known to exhibit non-Rayleigh speckle in the ultrasonic regime and are described more accurately using generalized speckle models (e.g. the generalized K-distribution model [44]). Using these generalized speckle models as a basis, it may be possible to extend the methodology presented here to the simulation of non-Rayleigh speckle through the introduction of coherent components, the use of low scatterer number densities, or the use of non-Rayleigh probability distributions on the scattering cross-sections.

Also of research interest are continued studies into three-dimensional flow reconstruction algorithms. We have shown through simulation that an algorithm based on vector projection breaks down in the presence of complicated flow patterns. It was hypothesized that this breakdown occurs due to off-axis interference but further studies are needed to understand this problem more thoroughly. In addition, reconstruction methods that have been introduced in the literature more recently, such as

the transverse oscillation method, can be tested and more thoroughly understood using simulation.

Finally, we are interested in incorporating specific transducer models into these simulation tools to tackle feasibility and optimization problems for capacitive micromachined ultrasonic transducers. While the addition of transducer and noise models has been alluded to in this work, the details of how best to incorporate these specific models will require further studies.

REFERENCES

[1] K. Dussik, "On the possibility of using ultrasound waves as a diagnostic aid," *Neurol. Psychiat.*, vol. 174, pp. 153–168, 1942.

[2] Staecker, "Public domain, commons.wikimedia.org/wiki/File%3{A}3dultrasound_20_weeks.jpg," June 2007.

[3] P. J. Lynch and C. C. Jaffe, "Licensed under CC:BY 2.5, www.yale.edu/imaging/echo_atlas/views/four_chamber.html," July 1999.

[4] Schomynv, "Licensed under CC:BY:SA 3.0, commons.wikimedia.org/wiki/File%3{A}TEE-Sonde.png," 2003.

[5] T. Bartel, S. Müller, A. Biviano, and R. T. Hahn, "Licensed under CC:BY:NC 3.0, www.ncbi.nlm.nih.gov/pubmed/24144789," Sept. 2013.

[6] L. Landini, R. Sarnelli, E. Picano, and M. Salvadori, "Evaluation of frequency dependence of backscatter coefficient in normal and atherosclerotic aortic walls," *Ultrasound in Medicine and Biology*, vol. 12, pp. 397–401, May 1986.

[7] B. I. Raju and M. A. Srinivasan, "High-frequency ultrasonic attenuation and backscatter coefficients of in vivo normal human dermis and subcutaneous fat," *Ultrasound in Medicine and Biology*, vol. 27, pp. 1543–1556, Nov. 2001.

[8] M. O'Donnell, J. W. Mimbs, and J. G. Miller, "Relationship between collagen and ultrasonic backscatter in myocardial tissue," *Journal of the Acoustical Society of America*, vol. 69, pp. 580–588, Feb. 1981.

[9] K. K. Shung, R. Sigelmann, and J. Reid, "Scattering of ultrasound by blood," *IEEE Transactions on Biomedical Engineering*, vol. BME-23, pp. 460–ï£ · 467, Nov. 1976.

[10] T. Szabo, *Diagnostic Ultrasound Imaging: Inside Out*. Biomedical Engineering, Elsevier Science, 2013.

[11] G. E. Tupholme, "Generation of acoustic pulses by baffled plane pistons," *Mathematika*, vol. 16, no. 02, pp. 209–224, 1969.

[12] P. R. Stepanishen, "Pulsed transmit/receive response of ultrasonic piezoelectric transducers," *Journal of the Acoustical Society of America*, vol. 69, pp. 1815–1827, June 1981.

[13] B. E. Treeby and B. T. Cox, "k-wave: Matlab toolbox for the simulation and reconstruction of photoacoustic wave fields," *Journal of Biomedical Optics*, vol. 15, no. 2, 2010.

[14] J. A. Jensen, "Linear description of ultrasound imaging systems," *International Summer School on Advanced Ultrasound Imaging*, 1999.

[15] S. Holm, "Ultrasim-a toolbox for ultrasound field simulation," *University of Oslo*, 2001.

[16] B. Piwakowski and B. Delannoy, "Method for computing spatial pulse response: Time-domain approach," *Journal of the Acoustical Society of America*, vol. 86, Dec. 1989.

[17] J. A. Jensen, "Field: A program for simulating ultrasound systems," in *10th NordicBaltic Conf. Biomed. Imaging, vol. 4, supplement 1, part 1:351–353*, 1996.

[18] J.-F. Synnevag, A. Austeng, and S. Holm, "Minimum variance adaptive beamforming applied to medical ultrasound imaging," in *2005 IEEE Int. Ultrason. Symposium*, vol. 2, pp. 1199–1202, Sept. 2005.

[19] A. Swillens, P. Segers, H. Torp, and L. Lø vstakken, "Two-dimensional blood velocity estimation with ultrasound: speckle tracking versus crossed-beam vector Doppler based on flow simulations in a carotid bifurcation model.," *IEEE Transactions on Ultrasonics, Ferroelectrics, and Frequency Control*, vol. 57, pp. 327–39, Jan. 2010.

[20] J. A. Jensen and N. Svendsen, "Calculation of pressure fields from arbitrarily shaped, apodized, and excited ultrasound transducers," *IEEE Transactions on Ultrasonics, Ferroelectrics, and Frequency Control*, vol. 39, no. 2, pp. 262–267, 1992.

[21] J. A. Jensen, "A model for the propagation and scattering of ultrasound in tissue," *Journal of the Acoustical Society of America*, vol. 89, no. 1, p. 182, 1991.

[22] J. A. Jensen, D. Gandhi, and W. O'Brien, "Ultrasound fields in an attenuating medium," *Proceedings of IEEE Ultrasonics Symposium*, pp. 943–946, 1993.

[23] K. Shung, "Ultrasonic characterization of biological tissues," *Journal of Biomechanical Engineering*, vol. 107, pp. 309–14, Nov. 1985.

[24] D. Fei and K. Shung, "Ultrasonic backscatter from mammalian tissues," *Journal of the Acoustical Society of America*, vol. 78, no. September 1985, pp. 871–876, 1985.

[25] F. D'Astous and F. Foster, "Frequency dependence of ultrasound attenuation and backscatter in breast tissue," *Ultrasound in Medicine and Biology*, 1986.

[26] X. Chen, D. Phillips, K. Schwarz, J. Mottley, and K. Parker, "The measurement of backscatter coefficient from a broadband pulse-echo system: a new formulation," *IEEE Transactions on Ultrasonics, Ferroelectrics and Frequency Control*, vol. 44, pp. 515–525, Mar. 1997.

[27] R. Wagner, S. Smith, J. Sandrik, and H. Lopez, "Statistics of speckle in ultrasound b-scans," *IEEE Transactions on Sonics and Ultrasonics*, vol. 30, pp. 156–163, May 1983.

[28] P. Shankar, "A model for ultrasonic scattering from tissues based on the k distribution," *Physics in Medicine and Biology*, vol. 1633, 1995.

[29] F. Destrempes and G. Cloutier, "A critical review and uniformized representation of statistical distributions modeling the ultrasound echo envelope," *Ultrasound in Medicine and Biology*, vol. 36, pp. 1037–51, July 2010.

[30] P. M. Shankar, "A general statistical model for ultrasonic backscattering from tissues," *IEEE Transactions on Ultrasonics, Ferroelectrics, and Frequency Control*, vol. 47, no. 3, pp. 727–736, 2000.

[31] G. M. Treece, A. H. Gee, and R. W. Prager, "Ultrasound compounding with automatic attenuation compensation using paired angle scans," *Ultrasound in Medicine and Biology*, vol. 33, pp. 630–642, Apr. 2007.

[32] T. Bartel, S. Müller, A. Biviano, and R. Hahn, "Why is intracardiac echocardiography helpful? Benefits, costs, and how to learn," *European Heart Journal*, vol. 35, pp. 69–76, Jan. 2013.

[33] I. Hein and W. O. Jr, "Current time-domain methods for assessing tissue motion by analysis from reflected ultrasound echoes-a review," *IEEE Transactions on Ultrasonics, Ferroelectrics, and Frequency Control*, 1993.

[34] D. H. Evans, J. A. Jensen, and M. B. Nielsen, "Ultrasonic colour Doppler imaging.," *Interface focus*, vol. 1, pp. 490–502, Aug. 2011.

[35] M. Fox, "Multiple crossed-beam ultrasound Doppler velocimetry," *IEEE Transactions on Sonics and Ultrasonics*, vol. 2, no. 5, pp. 0–5, 1978.

[36] M. Scabia, M. Calzolai, L. Capineri, L. Masotti, and A. Fort, "A real-time two-dimensional pulsed-wave Doppler system," *Ultrasound in Medicine and Biology*, vol. 26, no. 1, pp. 121–131, 2000.

[37] M. Arigovindan and M. Suhling, "Full motion and flow field recovery from echo Doppler data," *Medical Imaging, ...*, vol. 26, no. 1, pp. 31–45, 2007.

[38] G. E. Trahey, J. W. Allison, and O. T. von Ramm, "Angle independent ultrasonic detection of blood flow.," *IEEE Transactions on Biomedical Engineering*, vol. 34, pp. 965–7, Dec. 1987.

[39] M. Aderson, "Multi-dimensional velocity estimation with ultrasound using spatial quadrature," *IEEE Transactions on Ultrasonics, Ferroelectrics, and Frequency Control*, vol. 45, pp. 852–61, Jan. 1998.

[40] J. A. Jensen and P. Munk, "A new method for estimation of velocity vectors.," *IEEE Transactions on Ultrasonics, Ferroelectrics, and Frequency Control*, vol. 45, pp. 837–51, Jan. 1998.

[41] G. Montaldo, M. Tanter, J. Bercoff, N. Benech, and M. Fink, "Coherent plane-wave compounding for very high frame rate ultrasonography and transient elastography.," *IEEE Transactions on Ultrasonics, Ferroelectrics, and Frequency Control*, vol. 56, pp. 489–506, Mar. 2009.

[42] R. Chiao and L. Thomas, "Synthetic transmit aperture imaging using orthogonal golay coded excitation," *Ultrasonics Symposium, 2000 IEEE*, pp. 1677–1680, 2000.

[43] R. Y. Chiao and X. Hao, "Coded excitation for diagnostic ultrasound: a system developer's perspective.," *IEEE Transactions on Ultrasonics, Ferroelectrics, and Frequency Control*, vol. 52, pp. 160–70, Feb. 2005.

[44] E. Jakeman and R. Tough, "Generalized K distribution: a statistical model for weak scattering," *Journal of the Optical Society of America A, Optics and Image Science*, vol. 4, no. 9, pp. 1764–1772, 1987.